Observations of Tropical Cyclone Inner-Core Fine-Scale Structure, and Its Link to Intensity Variations

LÉO VINOUR,[a] SWEN JULLIEN,[a] ALEXIS MOUCHE,[a] CLÉMENT COMBOT,[a] AND MORGAN MANGEAS[b]

[a] *IFREMER, Univ. Brest, CNRS, IRD, Laboratoire d'Océanographie Physique et Spatiale, IUEM, Plouzané, France*
[b] *IRD/UMR ENTROPIE, Nouméa, New Caledonia, France*

(Manuscript received 14 August 2020, in final form 26 June 2021)

ABSTRACT: Tropical cyclone (TC) internal dynamics have emerged over recent decades as a key to understand their intensity variations, but they are difficult to observe because they are sporadic, multiscale, and occur in areas of very strong wind gradients. The present work aims at describing the internal structure of TCs, as observed with newly available satellite synthetic aperture radar (SAR) wind products, and at evaluating relations between this structure and the TC life cycle. It is based on a unique dataset of 188 SAR high-resolution (1 km) images, containing 15–47 images by intensity category. An extraction method is designed to retrieve and characterize the TC radial profile, its azimuthal degree of asymmetry, and the energy distribution in the eyewall and maximum wind areas. Vortex contraction and sharpening of the eyewall wind radial gradient with increasing TC intensity are observed, as well as a symmetrization of energy distribution around the vortex. Eyewall high-wavenumber structures show a dependence on the life-cycle phase, supporting previous findings discussing the vortex rapid evolution with onset and propagation of eyewall mesovortices and associated vortex Rossby wave generation. A machine-learning approach highlights that the eye shape and eyewall radial wind gradient fine-scale dynamics have the potential to improve the statistical prediction of TC intensity variations relative to the sole use of vortex-averaged parameters and synoptic information. The high-resolution radial and azimuthal coverage provided by SARs make these acquisitions a very valuable tool for TC research and operational application.

KEYWORDS: Tropical cyclones; Wind; Statistics; Radars/radar observations; Satellite observations; Classification

1. Introduction

Forecast and understanding of tropical cyclone (TC) life cycle has been a critical challenge of meteorological science for decades. The development of dynamical weather forecast models, and our increasing observational capacity from space have led to a better resolution of the synoptic steering flow and to subsequent improvements in TC track and maximum potential intensity forecasts (Miller 1958; Emanuel 1986, 1987; Elsberry et al. 2013). On the other hand, the forecast of TC intensity variations has seen much less progress (Cangialosi and Franklin 2019). TC intensification and mature-phase intensity variations are associated with multiscale interactions (interactions between very fine- and synoptic-scale processes (e.g., Elsberry et al. 2013), complex internal and stochastic dynamics in the inner core (e.g., Wang and Wu 2004; Montgomery and Smith 2014), and exchanges with the underlying ocean (e.g., Bender and Ginis 2000; Wada 2009; Jullien et al. 2014), which are more difficult to model and predict, and are not necessarily well understood.

TC intensification theories, developed since the 1960s (Charney and Eliassen 1964; Ooyama 1964, 1969; Emanuel 1986; Smith et al. 2009), are still debated. They assume that TC vortex intensification occurs through the spinup of tangential winds, which mainly takes place above the boundary layer (BL). There, the flow is assumed to be in gradient wind balance, and to converge due to eyewall deep convection causing tangential winds to increase (as angular momentum is conserved). In the BL, the assumed gradient wind balance is broken by surface friction, causing convergence of moist air that eventually releases latent heat when reaching the eyewall and provides fuel for deep convection (Emanuel 1986). Intensification thus occurs through a feedback between spinup above the BL, moisture inflow in the BL, and convection in the eyewall. A more recent study (Smith et al. 2009) also suggests that spinup could occur inside the BL due to supergradient winds present in the inner core, with the strongest winds thus located at the top of the BL and the inner core being partly decoupled from the outer core. Studying and observing the BL structure is thus crucial to better understand surface energy transfers and inner-core dynamics, such as wind spinup, gradient and supergradient balances, and convectively driven inflow, that drive TC intensification.

Intensity variations of the mature TC have also been thoroughly studied: while triggered by external events such as vertical wind shear or tropospheric troughs (Uhlhorn et al. 2014), they are also tightly connected to several internal processes mainly occurring in the inner-core, eye, and eyewall areas. Eye warming (Stern and Zhang 2013) and observed midlevel thermodynamic inversions within the eye (Jordan 1961; Willoughby 1998; Franklin et al. 1988) have been related to intensity variations as eye subsidence interacts with the eyewall convection and modifies the dynamical balance in the BL. Eye contraction is described as a supporting mechanism to vortex intensification and stabilization (Shapiro and Willoughby 1982;

Supplemental information related to this paper is available at the Journals Online website: https://doi.org/10.1175/JAS-D-20-0245.s1.

Corresponding author: Léo Vinour, leo.vinour@ifremer.fr

DOI: 10.1175/JAS-D-20-0245.1

Lee and Bell 2007). Secondary eyewalls (Holland et al. 2010; Willoughby et al. 1982) and eyewall replacements (Houze et al. 2007) have been observed as a result of TC vortex destabilization and progressive reestablishment after external events affecting the TC life cycle. A range of observational studies, mainly based on coastal (Macdonald 1968; Muramatsu 1986; Kuo et al. 1999) and airborne (Reasor et al. 2000; Corbosiero et al. 2006) dual-Doppler radar imagery, has also identified vortex Rossby waves (VRWs) as a progressive restoration process.

The VRW theory, first formalized by Montgomery and Kallenbach (1997), describes internal waves propagating along potential vorticity gradients that promote vortex axisymmetrization by propagating energy from the TC center to its periphery. In this context, a perturbation of the eyewall convection (most often caused by external shear) can cause a breaking of the eyewall vorticity ring, leading to emergence of eyewall mesovortices (Schubert et al. 1999; Kossin and Schubert 2001) These mesovortices modify the eye shape, induce mixing within the eye, and eventually organize, resulting in VRWs propagating around the eye and causing eye rotation. Then they propagate outward, generating inner rainbands of higher vorticity (Macdonald 1968), and possibly trigger the formation of outer spiral rainbands when reaching their stagnation radius (Montgomery and Kallenbach 1997; Chen and Yau 2001). Their propagation is suggested to allow dissipation of the center instability and reformation of the eyewall vorticity ring, thus enhancing eyewall convection and TC intensity. A complete review of VRW theory and their role in TC intensity variations is provided by Wang and Wu (2004).

Fast structural changes of TCs, associated with the fine-scale rapid evolution of the inner part of the eyewall, and subsequent VRW propagation certainly contribute to the difficulty of forecasting TC intensity changes. Usual operational statistical–dynamical forecast models (DeMaria and Kaplan 1994, 1999; Knaff et al. 2005; Knaff and Sampson 2009) use linear regression techniques to predict intensity changes from large-scale climatological fields (temperature, humidity, maximum potential intensity, shear, etc.), TC intensity, and rate of change at the forecast initial time. The observational limitations with regard to TC internal small scales (lack of spatial and temporal resolution) have prevented their use in such statistical models. Based on a numerical study, Judt et al. (2016) suggested that forecast errors rapidly grow on small scales, limiting their predictability. However, the tight relation between mesovortices generated in the eyewall inner edge, induced mixing and spinup within the eyewall (Schubert et al. 1999; Kossin and Eastin 2001; Nguyen et al. 2011) foresees toward a potential improvement of TC variation predictability with a better assessment of such fine-scale structures and associated dynamics.

The wide range of interacting processes that induce TC intensity variations, including external large-scale events, eye and eyewall instabilities, VRW generation and propagation, involve synoptic to turbulence scales ranging from days to seconds temporally, from hundreds of kilometers to meters spatially, and from the troposphere to the sea surface vertically. Observing the TC structure evolution associated with these intensity modulation processes thus requires a combination of high temporal and spatial resolution, together with a large coverage, and a cloud-penetrating technology. The definition of a sensor or a network of complementary sensors able to achieve comprehensive observations of TCs at global scale thus remains a challenge.

The most prevalent TC observation source is geostationary satellite imagery; it provides high-resolution, extended geographical and temporal coverage and is widely used for TC intensity monitoring and forecast (Dvorak 1975; Olander and Velden 2007). However, geostationary observations are limited to top-of-the-cloud information (as they operate in visible and infrared wavelength) and cannot directly retrieve the BL evolution. Other available satellite observations for wind measurements are those of L-band or multifrequency radiometers and scatterometers (cloud-penetrating microwave wavelength). They are able to provide a direct estimate of the wind speed at the ocean surface (Meissner and Wentz 2009; Zabolotskikh et al. 2015; Katsaros et al. 2002; Reul et al. 2017) and thus valuable information on the TC structure. However, they are limited by their spatial resolution (usually 40–50 km) preventing their use for studying the TC inner-core structure. Small-scale BL observations are thus usually only obtained with airborne Doppler radars, dropsondes, and ground-based radars. These observations provide high-resolution measurements in the BL (Marks 2003), but with limited geographic extent and sampling capacity: airborne observations have a very partial coverage of the azimuthal structure (Reasor et al. 2000; Uhlhorn et al. 2014), and time lags between passes that limit the temporal coverage, and coastal radars do not have access to the entire TC life cycle due to their limited radial extent.

The technology of synthetic aperture radars (SARs) provides an adapted complement to these techniques. It is indeed the only satellite remote sensing technique that allows probing the sea surface at very high resolution and can provide estimates of 2D wind fields with kilometer resolution (Katsaros et al. 2002). However, SAR data are not commonly used for TC observations for several reasons: 1) over open ocean there is no systematic SAR acquisition, and some of the acquisition modes do not allow for TC wind retrieval; 2) to date, the planning of TC acquisitions in the adequate mode is not a priority for SAR missions' objectives and is only performed on request and if other higher-priority acquisitions are not planned; 3) the wind retrieval from SAR images in TCs requests a dedicated treatment, which has only been recently developed (Zhang et al. 2016; Mouche et al. 2017); and 4) SAR data are currently not available in real time, limiting their potential use to postevent reanalysis only. Nevertheless, SAR data have been shown to allow the retrieval of several TC properties: TC center, eye shape (Lee et al. 2016; Du and Vachon 2003; Jin et al. 2014; Liu et al. 2014), rainbands and precipitation (Long and Nie 2017; Jin et al. 2017; Zhang and Li 2017), convective cells (Zhang and Li 2017), BL rolls (Foster 2005), and surface wind speed (Zhang et al. 2016; Zhang and Perrie 2017; Yang et al. 2017). Based on a set of 83 net radar cross section (NRCS) SAR acquisitions, Li et al. (2013) adopted a statistical approach to link

TC eye derived morphology to TC intensity. They associated a reduction of the eye extent and a decrease of the eye shape wavenumber asymmetry with an increase in intensity, thus observing the eye contraction and axisymmetrization with intensity. As most wind inversion algorithms under high winds are new or still under validation, most existing SAR studies have focused on surface roughness data for the estimation of TC properties (eye shape, BL rolls, rainbands, or mesovortices), and are often limited to weak TCs.

The present study takes advantage of a new consequent database of TC SAR observations, which has been gathered from two SAR missions (Sentinel-1 and *RADARSAT-2*) over a 4-yr period extending from 2016 to 2019. This database covers a wide range of TC cases. It has been used to set up a new wind inversion algorithm (Mouche et al. 2017) and has been validated against the International Best Track Archive for Climate Stewardship (IBTrACS), the National Oceanic and Atmospheric Administration (NOAA) airborne measurements, and the L-band radiometer wind estimations (Combot et al. 2020; Mouche et al. 2017, 2019). Based on this new consequent database of SAR wind speed retrievals in TCs, the present study describes a method developed to extract TC structural properties (e.g., eye and ring of maximum wind shapes, surface wind gradients), and energy repartition within the TC vortex (characterized through surface wind intensity spectral decomposition).

Our analyses then demonstrate the ability to describe and characterize, with such acquisitions, the TC inner core, through its radial profile, its azimuthal degree of asymmetry, and the energy distribution in the eyewall and maximum wind areas. These results have strong implications for operational and research applications, as the near-real-time estimation of typical TC characteristics (maximum wind speed, radius of maximum winds, inner-core and near-core wind gradients, vortex asymmetries), which can be used for TC forecasts, high-wave and storm-surge forecasts, and observational research on inner-core dynamics and intensity restoration processes. Our analyses also suggest potential use of our wind profiles for estimating mean wind profiles, or fitted 2D wind structures, which could be used as forcing for operational risk assessment or other research applications. A second objective of our statistical analyses is to investigate the importance of the fine-scale variability of the eyewall and area of maximum wind for understanding the TC intensity fluctuations, and their potential to improve our ability to dissociate intensification phases. As SAR acquisitions are snapshots, with a relatively sparse sampling, they do not allow for a continuous monitoring of each TC evolution and prevent for an estimate of the short-range dynamical changes in the internal structure. However, here we propose to evaluate their predictability potential by assessing the relation of TC SAR-extracted parameters (intensity, size, radial profiles, azimuthal degree of asymmetry and energy distribution) to the 12-h ongoing TC intensity change. An evaluation of their added value in an actual statistical forecast model is beyond the scope of this paper but may be an exciting perspective.

The paper is organized as follows. Section 2 describes the dataset and the method of processing of SAR images; section 3 then describes the TC radial and azimuthal structures and investigates their evolution as a function of TC intensity, with a focus on the inner-core and the eyewall area and compares these new SAR observations with previous studies. The benefit of observing these internal structural properties to depict the TC life cycle and its predictability is assessed in the last part of section 3, using a method based on machine-learning classification. Section 4 discusses our results and the technical limitations of our dataset, and in section 5 conclusions are drawn.

2. Data and methods

a. SAR dataset

The SAR dataset used in this study is the result of the Satellite Hurricane Observation Campaign (SHOC) started in 2016 by the European Space Agency (ESA). Following the first promising SAR observations made with *RADARSAT-1* in TCs (Friedman and Li 2000; Katsaros et al. 2000; Du and Vachon 2003), SHOC aims at programming acquisitions over TCs with Sentinel-1 and *RADARSAT-2* SAR missions based on TC track forecasts.

SAR is a side-looking microwave active sensor, which measures the backscatter signal to estimate sea surface roughness. The synthetic aperture principle consists in processing together the phase and amplitude of several consecutive acquired signals to build a synthetic along-track antenna much larger than the real one. The high sampling frequency and the synthetic aperture therefore provide a spatial resolution that ranges from 10 m to 1 km (depending on the acquisition mode). The drawback of SAR high resolution is that the raw data volume is very high, and consequently the satellite is not in continuous acquisition mode.

Both Sentinel-1 and *RADARSAT-2* are C-band SARs. The acquisitions are carried out in wide swath mode to encompass the whole TC structure, and in both co- and cross-polarization modes, which have been shown to complement one another in retrieving wind speed and direction. Indeed, as outlined by Mouche et al. (2017), the cross-polarization implemented on both Sentinel-1 and *RARDARSAT-2* is much more sensitive to high wind gradients, allowing a better resolution of the TC wind field (characterized by large wind gradients and wind speeds exceeding 35 m s^{-1}). On the other hand, cross-polarization is also more sensitive to noise (due to swath junctions or precipitation in the atmospheric column). The copolarization is thus used to validate or replace cross-polarized data in the low to moderate wind regimes and will help retrieving wind streaks for estimation of the wind direction. This latter capacity is, however, not fully implemented yet, and therefore, it is not available for the present study. The geophysical model functions used are CMod5n for copolarized and MS1A for cross-polarized data, as described in Mouche et al. (2017).

The validity of the SAR TC wind field database used in the present study was thoroughly evaluated against the NOAA airborne measurements using the Stepped Frequency Microwave Radiometer (SFMR), L-band radiometer wind estimations, and the IBTrACS by Mouche et al. (2017, 2019) and Combot et al. (2020). Mouche et al. (2017, 2019) described and validated the wind inversion algorithm against L-band radiometer data, and SFMR data. Combot et al. (2020) examined and validate the

SAR database [TC maximum wind intensity (V_{MAX}), radius of maximum winds (RMW), and characteristic 34-, 50-, and 64-kt (1 kt $\approx$ 0.51 m s^{-1}) wind radii (R34, R50, and R64)] against IBTrACS and SFMR data. Overall, these three papers showed an excellent agreement of the wind intensity retrieved from SAR with all compared datasets (IBTrACS, SFMR, and L-band radiometers). Combot et al. (2020) found a 0.87 correlation between SAR and best-track (BT) V_{MAX}, with an 8.76 m s^{-1} RMSE, and an even higher agreement with SFMR data (correlation of 0.9, RMSE of 4.85 m s^{-1}, and bias lower than 0.5 m s^{-1}). They associated the better agreement found with SFMR to BT estimate errors in cases of rapid intensifications (not well captured), or to eyewall replacements cycles. Some differences were also spotted as a consequence of rain artifacts in SAR data, which can cause inconsistent wind peaks. Fourteen percent of the cases were found to be significantly affected by rain. These cases were compared with Integrated Multisatellite Retrievals for GPM (IMERG) precipitation estimates, and maximum intensity was adjusted taking the maximum wind value only in low-rain-rate areas (<30 mm h^{-1}), yielding a mean difference of 6.2 m s^{-1} before and after V_{MAX} adjustment. Rain impacts on SAR wind retrievals are thus challenging issues and have to be kept in mind when analyzing the SAR wind field. However, they usually cause very localized anomalies, and the method that we developed in the present study was designed to minimize their potential impact on the results (see the appendix).

Combot et al. (2020) further evaluated the spatial structure of SAR retrieved wind fields by comparing the retrieved characteristic wind radii (RMW, R34, R50, and R64). RMW comparisons with SFMR revealed excellent agreement [correlation of 0.95 and bias of 3.5 km, except for the case of TC Florence (North Atlantic 2018)], and comparisons with BT showed larger discrepancies (0.47 correlation and RMSE of 25 km, improving to 11.6 km when discarding the cases of double eyewalls). BT RMW retrievals are, however, notoriously bad in the absence of aircraft data, as they are derived from indirect methods or low-orbit satellite missions using medium- to low-resolution observations. Additionally, radii associated with higher winds might have a higher temporal variability possibly not captured by the 6 hourly BT analysis. R34 and R50 comparison with BTs showed a correlation higher than 0.85, and a low normalized bias of ~3%, and of ~10% for R64 (larger differences in R64 being due to the same reasons as for RMW). Overall, Combot et al. (2020) showed the good performance of SAR in the retrieval of TC maximum intensity and structure parameters (RMW and characteristic radii) and advocated for their use as real-time and reanalysis observations for the improvement of best-track estimates. The present SAR dataset is thus considered to satisfactorily allow for TC surface wind field characterization, and will be shown, in this study, to offer a unique opportunity to capture inner- and near-core wind structure of the TC vortex, thanks to its high-resolution and spatial extent.

From the beginning of the SHOC campaign in 2016, 279 eye-matching TC acquisitions were gathered; 188 of these acquisitions successfully passed our parameter extraction procedure (described in the following section 2c) and were used in the present study. Other cases that were withdrawn are usually because of partially covered vortex structure, a too-large portion covered by land, or weak distorted TCs preventing parameter estimation. Figure 1 shows a wide range of TC characteristics (intensity, basin, position, size, intensification rate, and translation speed) represented in the 188-case dataset. These characteristics are computed from the images themselves, except for intensification rate and translation speed, which are computed from best-track data described in the following paragraph.

b. BT data

We use the IBTrACS (Knapp et al. 2010) that combines the BT data from various meteorological centers (regional specialized meteorological centers responsible for TC forecast in the different basins, and country agencies) into one common format. In a few cases, IBTrACS database does not completely cover the extent of an event. In these cases, the Automated Tropical Cyclone Forecast System (ATCF; Miller et al. 1990) is used to retrieve BT parameters. It may be noted that the most recent tracks from IBTrACS and ATCF are provisional, meaning that they have not been reprocessed with all available observations.

The BT position, radius of maximum wind (RMW_{BT}), and 34 kt radius (R34) are used for image processing (in particular for retrieving the TC eye and maximum wind areas). BT data [position and intensity ($Vmax_{BT}$)] are also used to characterize the TC life cycle, in particular the intensification rate, as no linear and continuous temporal dimension exists in SAR data due to a temporally sparse sampling of acquisitions. To provide the closest BT temporal parameter estimates for each SAR acquisition, the BT data are linearly interpolated at the acquisition time. The temporal resolution of BTs is limited to 3 h for IBTrACS and 6 h for ATCF, and the resolution in $Vmax_{BT}$ is respectively 1 m s^{-1} for IBTrACS and 5 m s^{-1} for ATCF data, yielding a limited precision of the interpolated tracks. We will show in the next section that a first important step in SAR image processing is to retrieve the TC center on the image itself, because the BT interpolated TC-center positions can be far from the true center. The intensification rate is defined as the time derivative of $Vmax_{BT}$ between $t - 6$ h and $t + 6$ h, t being the acquisition time.

In the next sections, parameters extracted from BTs are noted with a BT subscript (e.g., RMW_{BT}) to differentiate them from those retrieved from SAR.

c. Method of TC parameters extraction from SAR images

We designed a method to extract, from SAR-retrieved surface wind field, four characteristic azimuthal signals describing the TC: the maximum surface wind ring intensity and its shape, the eyewall surface wind gradient, and the eye shape. To do so, several steps are performed to ensure their best estimate, and to circumvent most of the errors in SAR measurements. The first step consists in masking potential areas of erroneous SAR wind speed, such as subswath intensity jumps (see blue lines in Fig. 2a) or local high heterogeneity not associated to wind but for instance to rain signatures (see gray contours in Fig. 2a). These masking steps are detailed in the appendix. The second

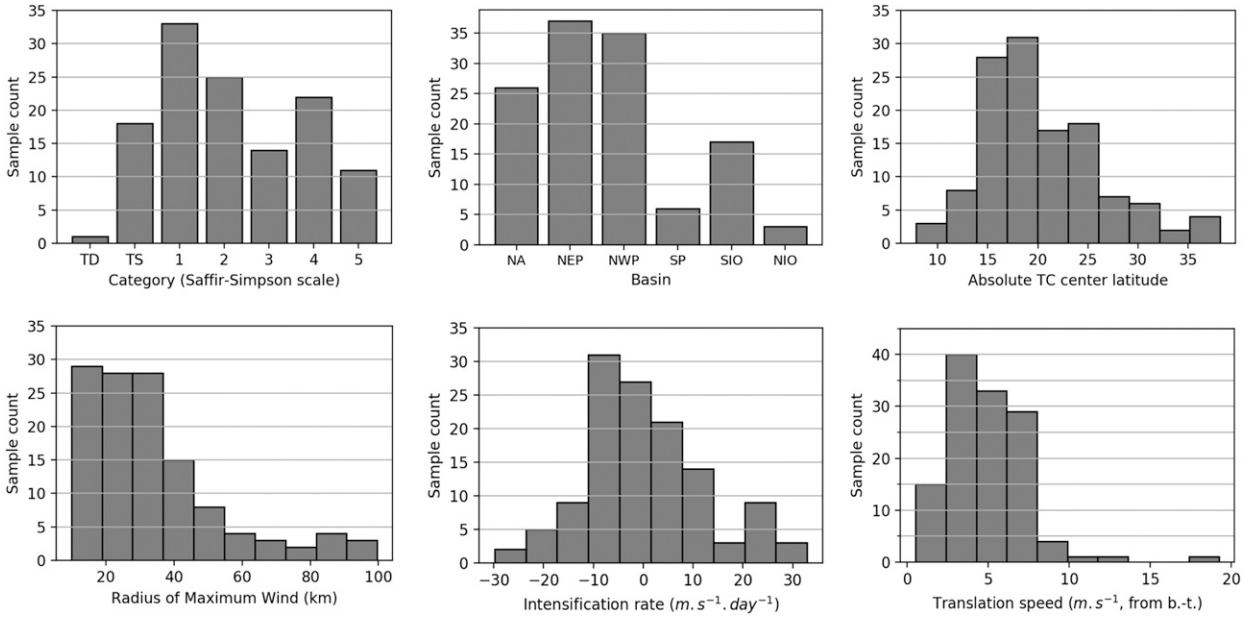

FIG. 1. Overview of the SAR TC database (number of samples) in terms of TC category, basin, absolute latitude, radius of maximum wind (km), intensification rate ($m\,s^{-1}\,day^{-1}$), and translation speed. The two latter are retrieved from best-track data, and the other parameters are retrieved from SAR images. Basin codes are the following: northern Atlantic (NA), northern eastern Pacific (NEP), northern western Pacific (NWP), southern Pacific (SP), southern Indian Ocean (SIO), and northern Indian Ocean (NIO).

step consists in detecting the TC center. This is performed using an iterative method that gradually approaches the TC center, first identifying the highest wind area (red contours in Fig. 2b), and then searching for a nearby low-wind-area centroid (light blue dot in Fig. 2b). The center position is finally defined as the centroid (yellow dot in Fig. 2b) of the maximum wind gradient contour around the low-wind centroid (black contour in Fig. 2b). The details of this iterative procedure are provided in the appendix.

1) EXTRACTING AZIMUTHAL SIGNALS

The SAR image is then projected and interpolated on a polar grid centered on the extracted TC center. The azimuthal resolution of the polar grid is set to 1°, and the radial vector is defined between 0 and 10 × $\mathrm{RMW_{SAR}}$ with a resolution matching the one from the original Cartesian grid of the image. The polar grid is geographically oriented with an easterly zero azimuth (the extracted signals are thus not oriented to the TC direction of motion).

Four characteristic azimuthal signals are extracted: two characterizing the TC intensity distribution, the eyewall wind gradient, and the maximum wind azimuthal distributions; and two characterizing the TC shape, the eye shape, and the maximum wind contour shape. The first signal is maximum wind distribution ($\mathrm{Vmax_{AZ}}$). The azimuthal distribution of maximum wind intensity is retrieved by extracting for each azimuth the maximum wind value. To avoid local outliers in the distribution, these maximum wind values are computed using a sliding average algorithm: for each azimuth, the profile used to compute maximum wind is averaged with its six closest neighbors. The retrieved signal is hereinafter denoted $\mathrm{Vmax_{AZ}}$. The second signal is maximum wind shape ($\mathrm{RMW_{AZ}}$). The contour of maximum winds is defined by the distance between the TC center and the maximum wind location for each azimuth. This azimuthal distribution of RMW is hereinafter referred to as $\mathrm{RMW_{AZ}}$.

The third signal is eyewall wind gradient (dV/dR_{AZ}). We define the eyewall as the region located between the minimum and the maximum of the second derivative of the radial profile between the TC center and $\mathrm{RMW_{AZ}}$ (see Figs. 3b,f) so that the eyewall does not include the "flat" wind areas located in the eye and near the peak of the wind profile. The azimuthal eyewall wind gradient, dV/dR_{AZ}, is then defined at each azimuth θ as the gradient $dV/dR_{\mathrm{AZ}}(\theta) = (\Delta V_{r_\theta}/\Delta r_\theta)_{r_{\theta\min} \to r_{\theta\max}}$, where V_{r_θ} is the radial wind speed profile for each azimuth, r_θ is the radius, and $r_{\theta\min}$ and $r_{\theta\max}$ are the values corresponding to the minimum and the maximum of the wind profile second derivative. We also define dV/dR_{EW} as the mean value of radial gradient in the eyewall computed on the azimuthally averaged wind profile. This parameter is thus a single value (instead of a 1D signal) estimating the average radial wind gradient in the eyewall.

The fourth signal, eye shape (hereinafter denoted $\mathrm{ES_{AZ}}$), is defined as a closed contour of wind located between the maximum radial wind gradient and the TC center. The maximum radial wind gradient is computed for a subset of radial profiles located at high-wind azimuths (corresponding to wind values between 99.5% and 99.9% of the image, denoted by black dots in Fig. 3). For each of these profiles, the wind value matching the maximum wind gradient is retrieved. These values are averaged and a wind contour matching this average value is extracted, along with nine other contours matching

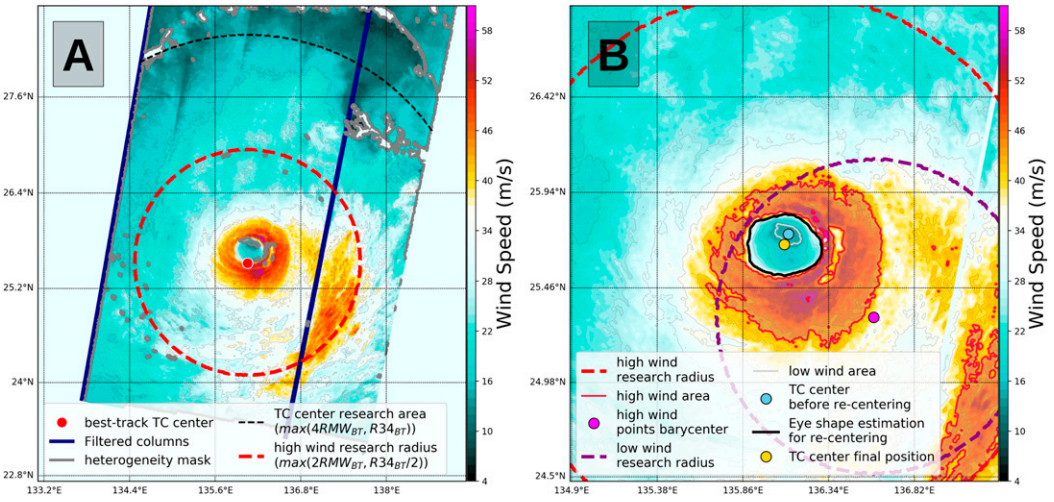

FIG. 2. (a) Illustration of the TC-center research algorithm for the case of TC Lionrock (western Pacific) observed with Sentinel-1 SAR on the 27 Aug 2016. (b) A zoom over the TC eye. The TC wind field ($m\,s^{-1}$) as retrieved from the SAR is shaded in (a) and (b). In (a) the heterogeneity mask (masking high gradient values of the backscatter signal) is represented with gray contours, the black-dashed circle denotes the radius at which the heterogeneity mask is removed, the subswath signatures are identified with dark-blue lines, and the red dot locates the interpolated BT TC center. The red-dashed circle in (a) and (b) denotes the first research area for theTC center. In (b) the detected high-wind points are contoured in red, their centroid is located with the magenta dot, the second research circle is featured by the purple-dashed line, the low-wind points are contoured in light gray, and their centroid is located with the cyan dot. The raw eye-shape signal is depicted by the black contour, and the final TC center is located with the yellow dot.

lower wind values (for cases with incomplete contours, see blue contours inside the eye in Fig. 3). The most exterior contour encompassing more than 70% of all azimuths is taken as the final shape.

These four previously extracted azimuthal signals are then smoothed by applying a third-order Butterworth filter with a critical frequency of 0.03 (an example is shown in Fig. 3b). A signal completion is also performed when the signals are partially cut by image border, by linearly interpolating the azimuthal signal.

2) COMPUTING VARIANCE AND SPECTRAL DECOMPOSITION

After normalizing the signals by their mean value, their variance is computed to characterize the overall asymmetry of the TC shape (relatively to a circle), and the distribution of energy (relatively to a homogeneous ring of wind). Then a wavenumber spectral decomposition is performed to assess the power level of each wavenumber composing the signal (Fig. 3). A recentering around the respective polygon centroid is applied to the two spatial signals (ES_{AZ} and RMW_{AZ}) prior to the spectral decomposition, as our purpose is to characterize the relative azimuthal distribution and not the decentering of the structure, which would strongly sign in wavenumber 1. The relative power levels therefore describe the shape characteristics (for instance, a relatively elliptical eye is characterized by the predominance of wavenumber 2 as shown in Figs. 3a,c, while a more polygonal eye is characterized by a broader spectrum with strong wavenumbers 3 and 5 as shown on the example of Figs. 3d,f). For the intensity signals ($Vmax_{AZ}$ and dV/dR_{AZ}), the spectral decomposition characterizes the energy distribution: the predominance of low wavenumbers indicates local maxima, while a broader spectrum with higher relative importance of high wavenumbers represents a more distributed energy.

The variance, being the sum of the spectral components, a large value can be associated either with a large amplitude of only one wavenumber (a distortion of the shape, or local energy maxima), or with a smaller amplitude but a larger number of components (which could describe a shape with more noise but closer to a circle in average). In practice though, the smoothing applied to azimuthal signals and the structure of the TC vortex causes the variance to be more likely associated with the predominance of large wavenumber amplitudes than to a broader spectrum as displayed in Fig. 3, where the upper eye shape is more elongated and has a higher variance than the lower one, which is more polygonal but is closer to a circle on average.

3) VORTEX-AVERAGED PROPERTIES

The maximum TC intensity (V_{MAX}) extracted from the SAR images is estimated as the maximum of the azimuthal maximum wind distribution, $V_{MAX} = \max(Vmax_{AZ})$. A mean radial profile is also computed for each image by performing an azimuthal average. A vortex-averaged RMW, as well as an averaged eyewall wind gradient, dV/dR_{EW}, and an averaged near-core radial gradient, $dV/dR_{NC} = (\Delta V_r/\Delta r)_{RMW \to 3RMW}$, are computed from this averaged radial profile. The three

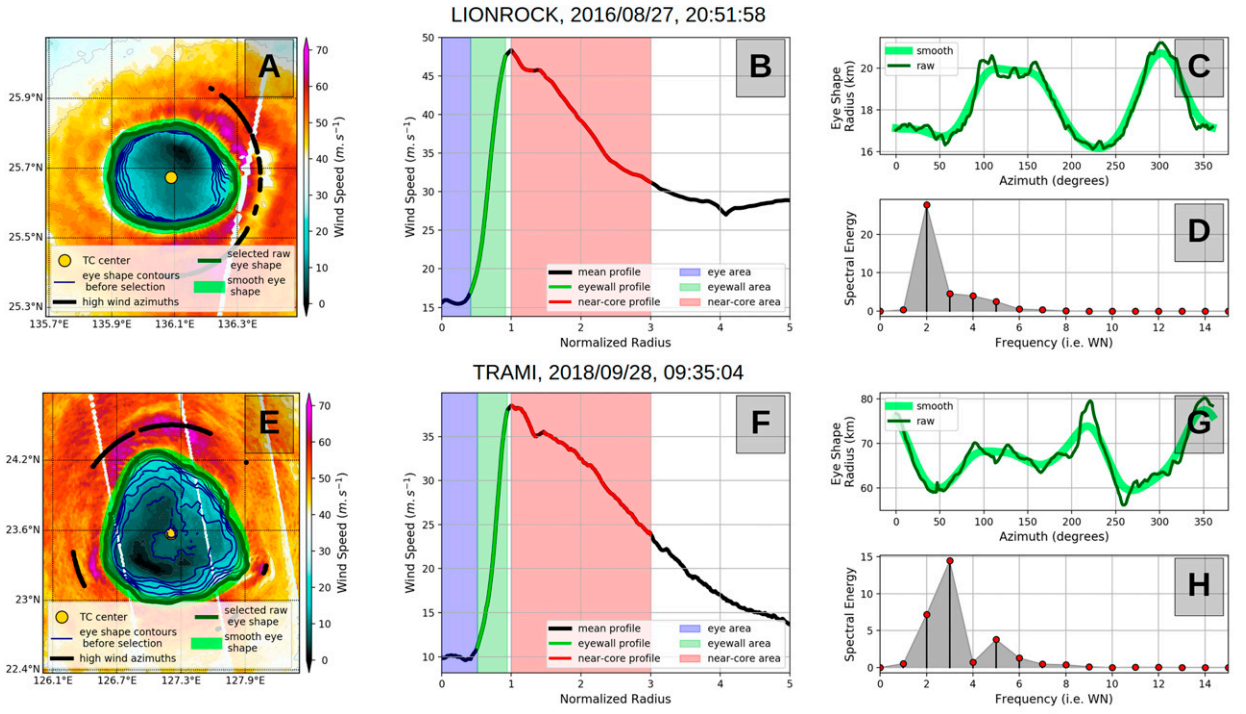

FIG. 3. Illustration of the azimuthal signal processing detailed in sections 2c(1) and 2c(2) (here for the eye shape) for two acquisitions on (top) Lionrock (western Pacific; 27 Aug 2016) and (bottom) Trami (western Pacific; 28 Sep 2018). (a),(e) The SAR 2D wind field and contour of the extracted eye shape (dark green line), and the smoothed eye shape (thick light-green line), with highlighted high-wind azimuths (black dots) used to compute the maximum radial gradient; the TC center is indicated with a yellow dot. (b),(f) Azimuthal-mean wind profiles with shaded characteristic wind areas (eye area in blue, eyewall in green, and near-core in red) and highlighted eyewall (green) and near-core (red) profiles used to compute mean gradient values. (c),(g) The azimuthal distribution of the eye shape, i.e., the radius between the eye-shape contour and the TC center. (d),(h) The spectral decomposition of the normalized smoothed eye-shape radius (the first 15 components are represented).

distinct areas of the radial profile, used to describe the inner core region of the vortex in the following, are thus

1) the eyewall area (green shading in Figs. 3b,f), which includes all points where the local radial gradient is higher than 20% of the distribution of radial gradient values for $R <$ RMW; this ensures that one considers the linear part of the eyewall and avoids the flat areas in the eye and near the maximum wind;
2) the eye area (blue shading in Figs. 3b,f), defined as the region between the TC center and the inner edge of the eyewall; and
3) the near-core area (red shading in Figs. 3b,f), which extends between the RMW and 3RMW; this definition of the near-core area is also used by Mallen et al. (2005) because it usually contains a critical radius used for the estimation of vortex resiliency.

The TC parameters extracted from SAR images are summarized in Table 1.

d. *Statistical classification of intensification rates*

The potential of SAR-extracted parameters to statistically predict TC intensification rate is assessed in the last part of our results [section 3c(2)] by using a statistical classification, the predictor being the intensification phase: intensification or decay. Two groups of intensification rates are identified: intensification rates above $5\,\mathrm{m\,s^{-1}\,day^{-1}}$ and decay rates under $-5\,\mathrm{m\,s^{-1}\,day^{-1}}$. The number of images used for this statistical classification is therefore 100 (over the 188 available images) because medium values of intensification rate (88 images between -5 and $5\,\mathrm{m\,s^{-1}\,day^{-1}}$ are ignored.

The SAR-extracted variables used as predictors for the classifications are the TC center absolute latitude, V_{MAX}, RMW, dV/dR_{EW}, and variance and percentages of explained variance of the five first wavenumbers of the four azimuthal signals ($\mathrm{ES_{AZ}}$, $\mathrm{RMW_{AZ}}$, dV/dR_{AZ}, and $\mathrm{Vmax_{AZ}}$). All of these variables have a correlation factor lower than 0.7, ensuring their independency. Only the near-core wind gradient, dV/dR_{NC}, was discarded from the analysis, due to its too large correlation with the eyewall gradient. Given the limited amount of samples (100) and the elevated number of variables (28) composing our dataset, an evaluation of the incremental added value of each variable was not possible. We thus designed a method to estimate the relative contribution of each variable to discriminate intensifications versus decays. Figure 4 illustrates the flowchart of this method.

The first step consists in reducing the number of variables (initially 28) by dividing the dataset into four groups based on

TABLE 1. Table summarizing the TC parameters extracted from the SAR images, as described in section 2c.

SAR-extracted parameters abbreviation	Brief description
$\mathrm{Vmax_{AZ}}$	Max wind intensity at each azimuth
$\mathrm{RMW_{AZ}}$	Radius of max wind speed at each azimuth
dV/dR_{AZ}	Eyewall wind gradient at each azimuth: $dV/dR_{\mathrm{AZ}}(\theta) = (\Delta \mathrm{V}_{r_\theta}/\Delta r_\theta)_{r_{\theta\min} \rightarrow r_{\theta\max}}$
$\mathrm{ES_{AZ}}$	Eye shape, defined as outermost closed contour of wind located between the max radial wind gradient and the TC center
V_{MAX}	Vortex max wind intensity: $V_{\mathrm{MAX}} = \max(\mathrm{Vmax_{AZ}})$
$\mathrm{RMW_{SAR}}$ or RMW	RMW of the mean vortex (i.e., averaged azimuthally)
dV/dR_{EW}	Vortex eyewall wind gradient: Eyewall gradient of the azimuthally averaged wind profile: $dV/dR_{\mathrm{EW}} = (\Delta\overline{V_r}/\Delta r)_{r_{\min} \rightarrow r_{\max}}$
dV/dR_{NC}	Vortex-averaged near-core radial gradient: $dV/dR_{\mathrm{NC}} = (\Delta\overline{V_r}/\Delta r)_{\mathrm{RMW} \rightarrow 3\mathrm{RMW}}$

the four azimuthal signals: $\mathrm{ES_{AZ}}$, $\mathrm{RMW_{AZ}}$, dV/dR_{AZ}, and $\mathrm{Vmax_{AZ}}$. Each subgroup contains the variance and the five first wavenumbers explained variance percentages of the given azimuthal signal, as well as the vortex-averaged properties (TC-center absolute latitude, V_{MAX}, RMW, and dV/dR_{EW}). A random variable is added to each group as a control variable, yielding four groups of 11 variables. Then, to further reduce the number of variables for the classification (number of samples versus variables issue), random combinations of 5 variables among the 11 in each group are classified separately; 330 random combinations and associated classifications are performed for each group.

The classification itself is performed using 10 usual machine-learning models (they are detailed in the fourth column of Fig. 4). These models feature a wide range of different methods of machine learning, including regression methods, tree classifiers or neural nets. These different models allow one to take into account a wide range of possible relations between variables, including nonlinear relations. The classification is performed with a bootstrap method (learning on 80% of the dataset and testing the remaining 20%, then iterating five times with an exclusive 20% each time).

The average prediction score is obtained for each combination of variables by averaging the 10 models' prediction scores. Combinations are then sorted by order of performance, and the best combinations are detailed.

3. Results

a. *TC vortex parameters and radial profile as observed with SAR*

The kilometer-resolution SAR surface wind retrieval allows a detailed 2D characterization of the TC inner-core region, the most intense area of the TC vortex. First, maximum wind speed (V_{MAX}) and averaged RMW, extracted from the SAR images, are analyzed and compared with previously

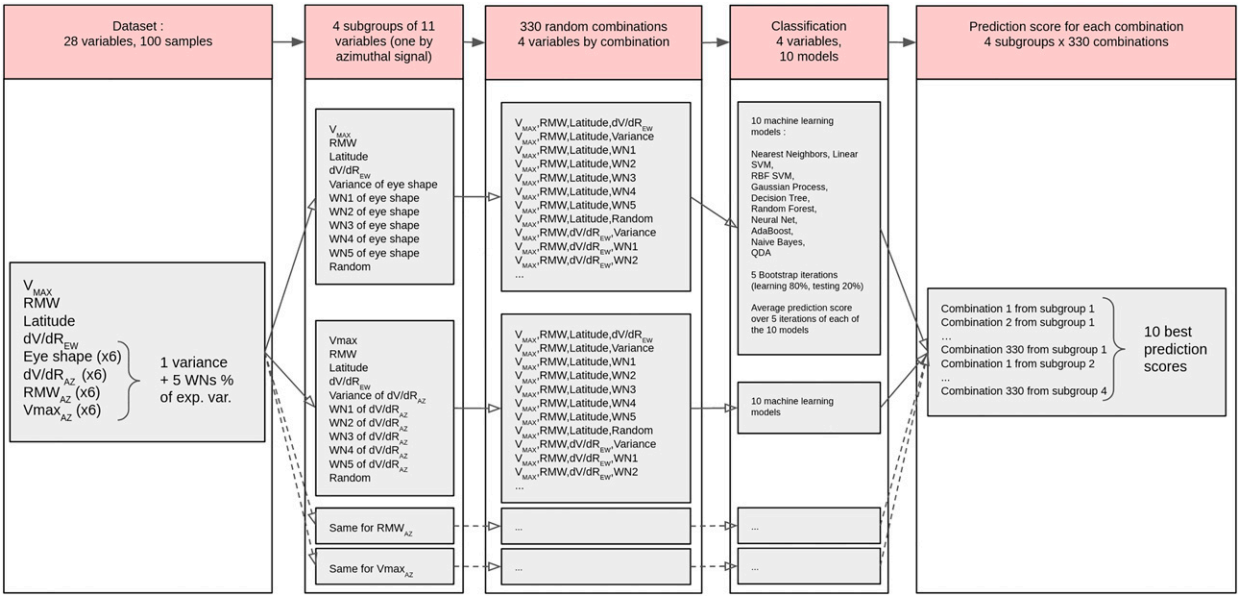

FIG. 4. Flowchart detailing the different steps of the statistical classification method. Red boxes depict the steps, and underlying gray boxes detail the dataset composition at each of these steps.

published results, and then a detailed description of the radial and azimuthal wind structures is assessed.

1) MAXIMUM WIND SPEED (V_{MAX}) AND RMW

The relationship between SAR-derived V_{MAX} and SAR-derived RMW is illustrated in Fig. 5a. In agreement with previous results from airborne and SAR measurements (e.g., Shea and Gray 1973; Weatherford and Gray 1988; Li et al. 2013; Combot et al. 2020), the RMW shows a decreasing trend, along with a decreasing variability as intensity increases: RMW extends from 10 to 100 km for TCs weaker than category 3 (50 m s^{-1}), while it is restricted to values lower than 50 km for stronger TCs (above category 3). This RMW decreasing trend with intensity can be associated with the eye contraction process described as contributing to TC intensification (e.g., Shapiro and Willoughby 1982; Stern et al. 2015).

The variability of RMW values observed for moderate (<category 3) TCs is very large whereas that for intense (≥category 3) TCs is smaller, and therefore we separate the following analyses into three TC groups: moderate and large TCs (V_{MAX} < category 3; RMW ≥ 50 km), moderate and small TCs (V_{MAX} < category 3; RMW < 50 km), and intense and small TCs (V_{MAX} ≥ category 3; RMW < 50 km). The RMW histograms of these three categories are shown in Fig. 5b. The moderate TC distribution features a relatively clear distinction between the moderate small and moderate large categories at 50 km, whereas intense TCs display RMWs distributed between 10 and 50 km with more numerous TCs in the lowest RMW categories. The standard deviations for both small moderate and intense TCs are similar (~13 km), and large moderate TCs have a larger spreading (standard deviation = 31.5 km), partly explained by the lower number of events in this category.

The events lying outside the overall standard deviation in Fig. 5a mostly belong to this moderate large category and are usually associated with highly asymmetrical TCs (see the online supplemental material), for which high winds are mostly confined to one sector of the TC vortex. It can be noted that these cases are particularly challenging for RMW retrieval in BT data, which often provide erroneous too low estimates of the RMW (see the online supplemental material), whereas our SAR retrieved RMW seems to be more faithfully estimated.

2) RADIAL WIND PROFILE

From the 188 SAR images of our dataset, we compute the average radial wind profile for each TC category (Fig. 6a). It shows a strong dependence on TC intensity, with tropical storms (TS, blue curve) having an almost linear profile between the center and the RMW, and strongest TCs (orange and red curves) having a so-called U-shape profile separated in two regions, the eye with a constant low wind value and the eyewall with a sharp wind gradient. The eyewall area, denoted by square (inner) and diamond (outer) markers in Fig. 6a, tends to move toward the maximum wind area with increasing category. More intense TCs thus have a maximum gradient closer to their RMW, and a wider eye. These observations are consistent with theoretical results that suggest that the eye formation and sharpening of the eyewall radial wind profile act as stabilizing processes to the TC, favoring its intensification to high

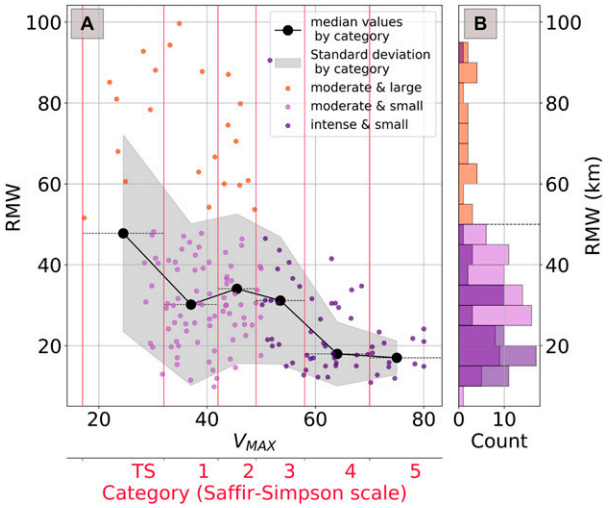

FIG. 5. (a) Distribution of SAR-extracted radius of maximum wind (RMW) as a function of maximum wind value V_{MAX}. Dots represent individual images, the black line features the binned median value by category (with horizontal lines indicating the bin extent), and the gray shading gives the corresponding standard deviation. Dot colors denote the division in three groups: moderate and large TCs (V_{MAX} < category 3; RMW ≥ 50 km), moderate and small TCs (V_{MAX} < category 3; RMW < 50 km), and intense and small TCs (V_{MAX} ≥ category 3; RMW < 50 km). (b) Histogram of RMW values for the three aforementioned groups.

categories. The theoretical results of Schubert and Hack (1982) indeed showed that the sharper the eyewall wind profile is, the stronger are the convective heating in the eyewall, the subsidence in the eye, and the inertial stability of the vortex.

To further characterize the eyewall wind gradient and its sharpening, it is compared with the Rankine vortex approximation, which assumes a solid-body rotation and a linear profile between $V = 0$ m s^{-1} at $R = 0$ and $V = V_{MAX}$ at $R =$ RMW. As detailed in section 2c(3), the eyewall wind gradient, dV/dR_{EW}, is computed over the quasi-linear region of the eyewall (delimited by the green shading in Figs. 3b,f) avoiding the flattened areas in the eye and close to the wind peak. Figure 6b shows that dV/dR_{EW} progressively departs from the Rankine vortex approximation as intensity increases, with a superlinear rate in binned average values. The spreading denoted by the interquartile range also increases with intensity and is the highest for category 5 TCs (though partly explained by the lower number of samples). As previously suggested (Fig. 5), moderate TC categories can be separated into two subcategories depending on their RMW. Large TCs show a gentler eyewall radial wind gradient (purple curve) in average relative to smaller TCs (orange curve) for a given intensity.

The progressive increase of the difference between the eyewall wind gradient and the Rankine approximation, as well as the separation between the two RMW subcategories and outward displacement of the eyewall area, highlight the fact that small and intense TCs have on average a relatively wider eye with respect to their RMW (e.g., the eye external border and RMW are relatively closer to each other), and a sharper

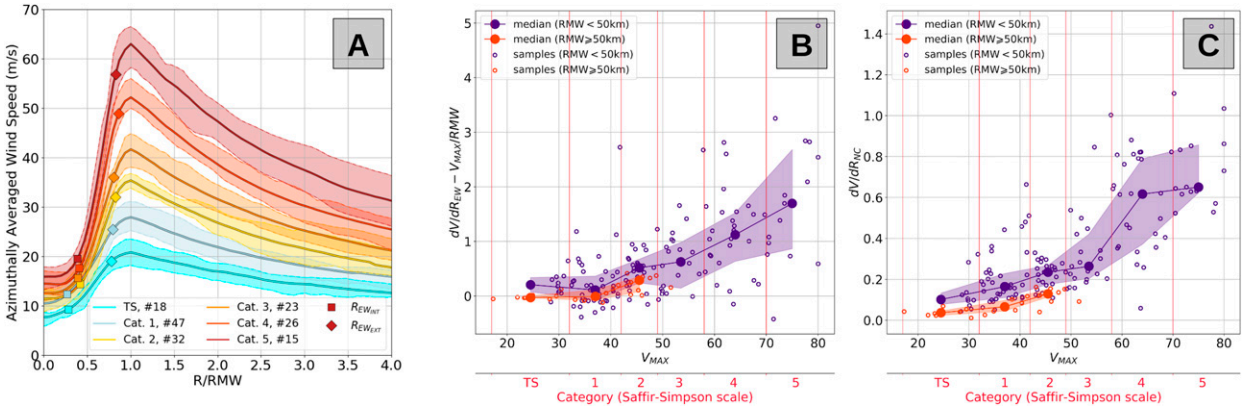

FIG. 6. (a) Mean radial wind profiles computed by TC category (Saffir–Simpson). Colored shading indicates the upper and lower quartiles for each profile, and the number of samples by category (''#'') is indicated in the legend. The x axis is normalized by the RMW. Symbols on the profiles denote mean positions of the eye inner and outer edge by category. (b) Difference between the eyewall radial wind gradient and the Rankine vortex wind gradient approximation: $(dV/dR)_{EW} - V_{MAX}/RMW$, as a function of V_{MAX} ($m\,s^{-1}$). Small open circles represent individual images, thick lines with large dark dots and shaded areas respectively denote the binned median and quartiles by category. Colors represent two subcategories of RMW: RMW < 50 km in orange and RMW ≥ 50 km in purple. (c) As in (b), but for the near-core radial wind gradient $(dV/dR)_{NC}$.

radially normalized eyewall wind profile than weaker and larger TCs. However, the large spreading of the data at strong intensity (Fig. 6b) also denotes a diversity of inner-core situations with a few very intense TCs not having the typical U shape with a strong eyewall radial gradient and a clearly separated eye. Kossin and Eastin (2001) also observed, in two aircraft sampled TCs, the existence of two distinct regimes of eyewall dynamics, one being characterized by a well-formed eyewall with a clear eye, and the second more similar to a Rankine-like vortex with increased horizontal mixing within the eye. They showed that the TC vortex can alternate between these two regimes in very short time ranges (1 h) and linked these transitions to important thermodynamic changes within the vortex structure. Nguyen et al. (2011) also documented such transitions modeling Hurricane Katrina and showed that U-shape profile phases were associated with faster intensifications. These two latter studies, as well as Schubert et al. (1999) and Kossin and Schubert (2001) further discussed how these profile transitions are related to the formation of eyewall mesovortices and subsequent vorticity mixing within the eye and VRW generation. The shape of the radial wind profile thus also depends on evolution of eyewall mesovortices. These aspects will be further examined in the next section, which describes the azimuthal structure and repartition of energy within the observed TCs.

To complement the study of the radial structure, the near-core radial gradient, $(dV/dR)_{NC}$, in the outer vicinity of the RMW (gray shaded area in Fig. 6a), is also computed (Fig. 6c). This near-core area is directly linked to the broadness of the primary circulation, also associated with the strength of the TC (Weatherford and Gray 1988), and has also been shown to characterize the vortex resiliency to external forcing (Mallen et al. 2005). The near-core radial gradient in our database is found to increase with TC intensity (Fig. 6c). A stronger increase is observed for TC categories 2–5 than for lower TC categories. As for the eyewall wind gradient, at a given intensity, the larger TCs (RMW ≥ 40 km) have a weaker near-core radial wind gradient. Overall, both eyewall and near-core wind gradient analyses illustrate an increased contraction of the high-wind area toward the RMW for more intense TCs. The fact that both gradients increase superlinearly on average with intensity shows that these trends of sharpening and contraction are accentuated in stronger TCs.

b. *Azimuthal TC structure and distribution of energy: Insights from SAR*

The radial profile analysis has provided an azimuthally averaged view of the TCs showing that stronger TCs tend to have a wider eye, a sharper eyewall radial wind profile, and a smaller, more contracted vortex. However, vortex asymmetry and azimuthal repartition of energy have been shown to be important components of the intensification mechanisms [cf. asymmetric theories of intensification reviewed by Montgomery and Smith (2014)]. We therefore extract the TC eye and RMW shapes to describe the spatial asymmetry (in comparison with a circle), and the eyewall wind gradient and maximum wind for each azimuth to describe the intensity distribution around the vortex.

Figures 7a and 7b show decreasing variances of ES_{AZ} and RMW_{AZ} for increasing TC categories, denoting an axisymmetrization of TCs with increasing intensity. The large TCs (purple in Fig. 7) feature higher mean values and larger spreading of variances than smaller TCs. These results suggest that axisymmetrization is a condition for TCs to reach category 4 or above, in addition to contraction of the structure, and sharpening of the eyewall radial wind profile.

The variances of eyewall wind gradient and maximum wind speed found around the vortex (Figs. 7c,d) also show decreasing trends with TC intensity, illustrating that in addition to the vortex axisymmetrization, the amplitude distribution is homogenized when intensity increases. To further describe this energy distribution, a wavenumber spectral decomposition is performed on the azimuthal eyewall wind gradient and

maximum wind signals [see methods section 2c(2)]. The wavenumbers (WNs) are gathered into three groups: low WNs (1 and 2), which represent the main components of TC asymmetry including signature of translation speed and planetary vorticity; medium WNs (3–5), which represent smaller-scale asymmetries not necessarily related to large-scale interactions; and high WNs (6–180), which describe the spreading of energy toward the tail of the spectrum but have been much less studied, as they are more difficult to observe and may be impacted by noise in the observations (in our case in SAR wind speed estimates).

Figure 8 shows a distinct evolution of the eyewall wind gradient and the maximum wind decompositions with TC intensity. On one hand, the maximum winds (green curves) feature a transfer of energy between low and high WNs, with WNs 1–2 explaining 65% of the variance at low intensity and decreasing to 55% at category 5, while medium and high WNs explained variances respectively increase from 23% to 25% and from 12% to 18%. On the other hand, the eyewall radial wind profile sharpness (blue curves), although showing a small transfer of energy from WNs 1–2 to WNs 3–5 between category <1 and category 3, has a much more balanced distribution with similar WN levels at weak and strong TC intensity. The energy distribution thus appears less related to the TC intensity in the eyewall than in the maximum wind area. The energy in the maximum wind area tends to be localized in one or two maxima for weak TCs and to homogenize for stronger TCs, while the eyewall sharpness is already more homogeneously distributed for weak TCs. The broader energy spectrum of the eyewall could also indicate the presence of mesovortices that may locally modify the vorticity mixing between the eye and the eyewall and thus the energy distribution, as discussed in the studies of Schubert et al. (1999), Kossin and Schubert (2001), and Nguyen et al. (2011). This highlights that the dynamics of the eyewall are not directly coupled with the maximum wind area and may have a separate behavior.

c. *Linking SAR-extracted characteristics to TC intensification*

In the previous section, we have depicted the TC radial surface wind profile, as well as the azimuthal characteristics of the eye and maximum wind ring shapes, and the azimuthal distribution of energy around the vortex. We have in particular highlighted that very intense TCs feature specific properties (sharper eyewall, more contracted and axisymmetric vortex, broader energy spectrum), which we have suggested could promote or constrain TC intensification. However, we have not yet assessed their direct relation with the intensification rate. This is the purpose of the next sections. As SAR acquisitions are snapshots, with a relatively sparse sampling, they do not allow for a continuous monitoring of each TC evolution, and the fine-scale structures observed in SAR images are certainly related to high-frequency intensity changes. We, however, here try to evaluate if SAR-extracted TC parameters allow to better characterize the TC life cycle and its intensity changes on relatively large time scales (12 h), in the view of assessing the potential use of SAR images for TC forecast issues and statistical models. The intensification rates are here computed from BT data and over a 12 h time window (from 6 h before to 6 h after the TC SAR acquisition), and are separated into three classes or phases: intensifying ($>5\,\mathrm{m\,s^{-1}\,day^{-1}}$), stable (between -5 and $+5\,\mathrm{m\,s^{-1}\,day^{-1}}$), and declining ($<-5\,\mathrm{m\,s^{-1}\,day^{-1}}$).

1) LIFE-CYCLE VARIATIONS

Figure 9 shows the distribution of the eyewall radial gradient in comparison with that of a Rankine vortex (Fig. 9a), and of the near-core radial gradient (Fig. 9) with respect to both V_{MAX} (x axis) and intensification rate (y axis). Both gradients show a strong dependence on intensity, as already illustrated in Fig. 6. In addition, a dependence on intensification rate is also notable. At a given intensity, higher gradients tend to be associated with higher intensification rates. Although the dependence is clearly lower than with intensity (eyewall and near-core gradient cross correlation with intensity are respectively 0.65 and 0.76, and with intensification rate 0.27 and 0.21), this mean trend indicates that, the faster a TC intensifies, the sharper its eyewall and near-core profiles. This is consistent with previous findings from Schubert et al. (1999) and Nguyen et al. (2011) showing that more U-shaped eyewall profiles associated with ring-like vorticity distribution favor rapid intensification. The trend to a sharper near-core and eyewall for intensifying TCs also indicates a reduced broadness of the primary circulation, which has been suggested to confer lower resiliency of the vortex to wind shear events (Reasor et al. 2004; Mallen et al. 2005).

The TC asymmetry, characterized by the azimuthal normalized variances of shape (eye and RMW) and energy distribution around the vortex (eyewall sharpness and maximum wind), does not show any direct relationship with the intensification rate (IR; not shown). However, a separation into different life-cycle phases reveals several noticeable features (Fig. 10). Intensity troughs (IR negative before, and positive after acquisition time, cyan bars) are notably more symmetric and homogeneous than other life phases, while the most asymmetric and heterogeneous phases are decline (negative IR before and after acquisition time, green bars) and intensification (positive IR before and after acquisition time, violet bars). An analysis of stronger TCs only (≥category 3) highlights a higher asymmetry of declining TCs over intensifying ones (not shown). The significant difference between declines and troughs shows the importance of vortex symmetry in the intensification process: both phases correspond to a negative intensification rate before acquisition, but TCs that reintensify are much more symmetric than TCs that continue to decline. The asymmetry associated with intensity peaks (IR positive before acquisition time and negative after, yellow bars) is higher than that of intensity troughs, which might be quite surprising at a first glance, as peaks are usually more intense phases than troughs, and as more intense TCs have been shown to have a higher symmetry (see Fig. 7). However, this result is interesting as it might suggest that the observed asymmetry could be a predictor of the subsequent decline after a peak. Intensity peaks are often perturbed and unstable life-cycle phases, where interactions of the vortex with its environment (shear, SST, islands) would result in

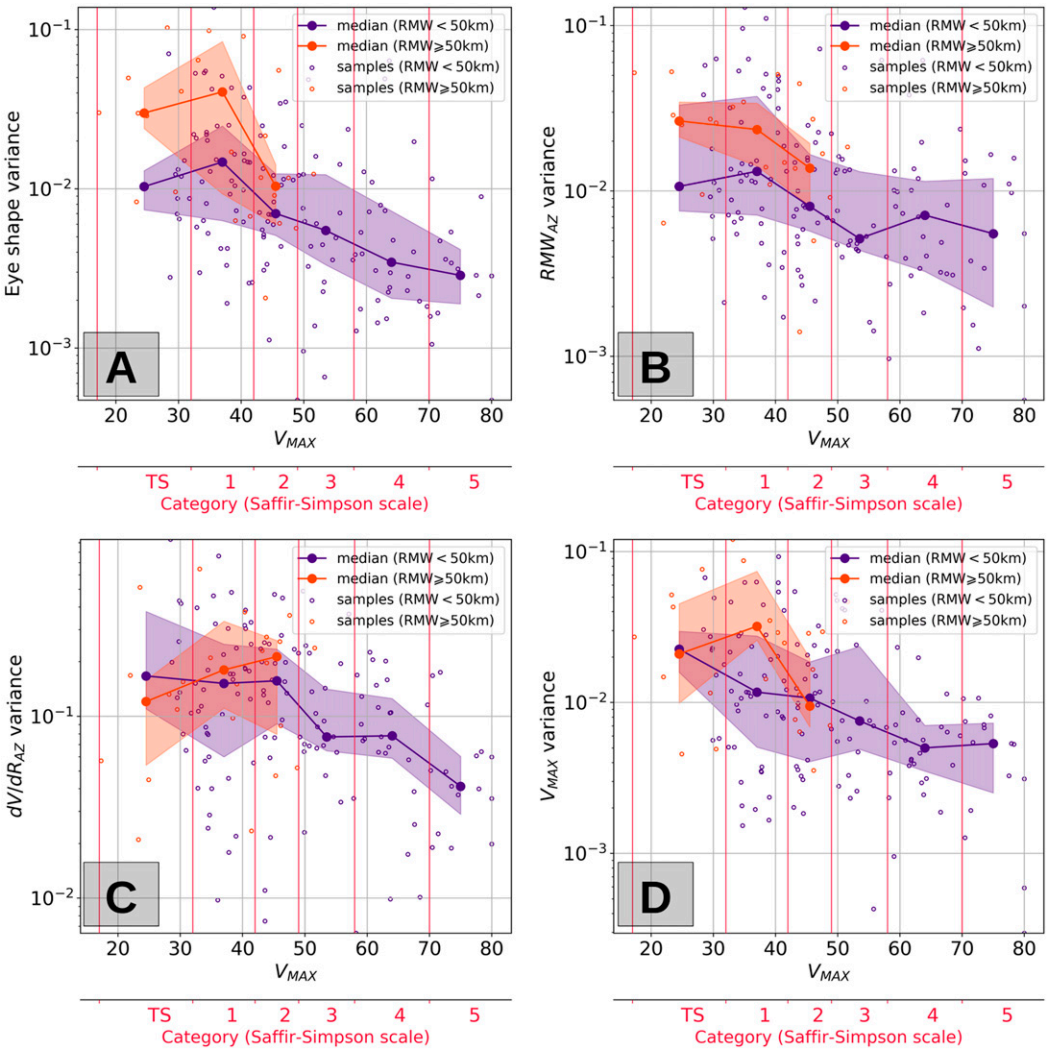

FIG. 7. Lognormal distribution of normalized variance of four azimuthal signals as a function of maximum wind: (a) eye shape, (b) RMW_{AZ}, (c) dV/dR_{AZ}, and (d) $Vmax_{AZ}$. Small open circles represent individual images; thick lines with large dark dots and shaded areas respectively feature the binned median and quartiles. Colors represent two subcategories of RMW: RMW < 50 km in orange and RMW ≥ 50 km in purple.

their following decline. These interactions may consequently enhance the internal activity.

2) MACHINE-LEARNING CLASSIFICATION: CONTRIBUTION OF FINE-SCALE EXTRACTED WIND STRUCTURES

From a predictability perspective, we assess the potential contribution of SAR-extracted TC parameters to a machine-learning statistical classification of positive ($>+5\,m\,s^{-1}\,day^{-1}$) and negative ($<-5\,m\,s^{-1}\,day^{-1}$) intensification rates. The method described in section 2d and Fig. 4 is applied to evaluate the prediction score of different combinations of extracted variables. The 10 best combinations are shown in Fig. 11. For each combination, the score is an average over the 10 different machine-learning algorithms.

Interestingly, only a few subsets of the 28 variables used as predictors appear in these 10 best combinations: the latitude of the TC center, the RMW, two components of the eye-shape decomposition (WNs 4 and 5), and several parameters characterizing the eyewall wind gradient (its mean value dV/dR, its azimuthal variance, and its WNs 1, 2, and 5). The latitude of the TC center is the most prominent parameter, appearing in each of the 10 best combinations. The typical life cycle of TCs with an intensification in the tropical latitudes and a decay in the midlatitudes explains this prominence. The RMW is the second most frequent parameter appearing in 8 or the 10 best combinations. RMW may also be associated with the typical life cycle as it is influenced by the planetary vorticity, but we also showed in section 3a(1) that the RMW is strongly associated with the intensity of the cyclone, and we suggested that this might be related to vortex contraction processes during intensification. This seems to be also supported by the strong contribution of the eyewall radial wind profile sharpness

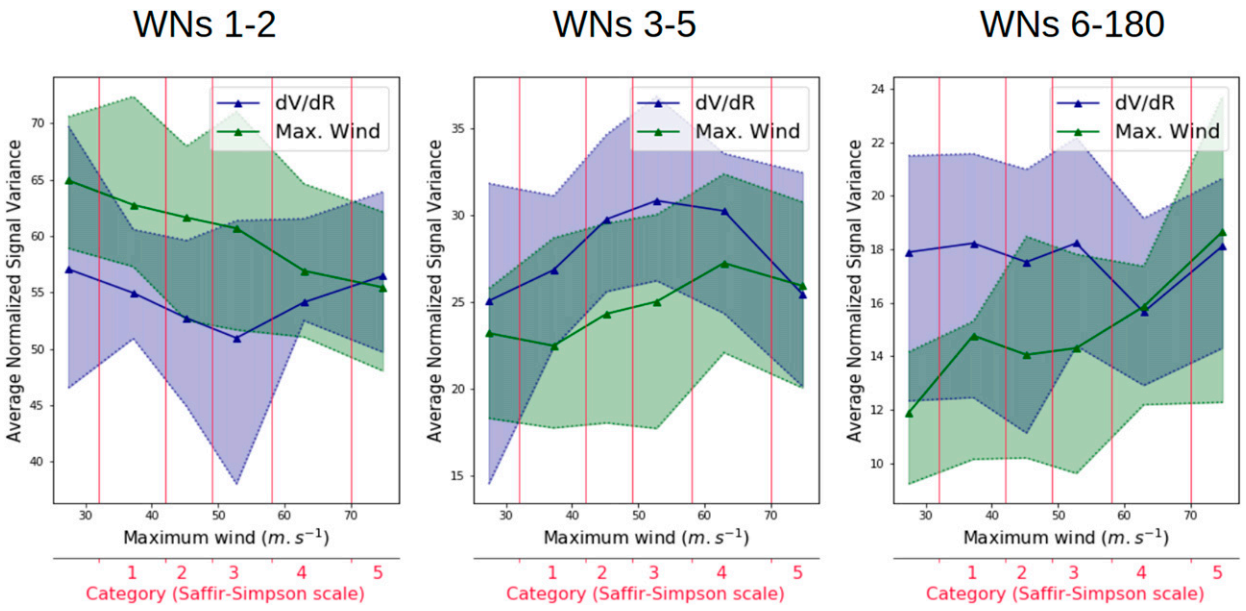

FIG. 8. Percentage of variance explained by wavenumbers (a) 1 and 2, (b) 3–5, and (c) 6–180 for dV/dR_{AZ} (blue) and $Vmax_{AZ}$ (green) azimuthal signals as a function of TC category. Thick lines and shaded areas respectively denote the binned median and quartiles.

(dV/dR) in the classification, which appears in numerous combinations through its different components (mean value, azimuthal variance, WN decomposition). Notably, high WNs of the eyewall wind gradient and of the eye shape are majorly represented in the best combinations (e.g., WN 5 is present in respectively six and four combinations for the eyewall gradient and the eye shape). These wavenumbers correspond to small-scale dynamic processes in the eyewall such as convective bursts and mesovortices (Schubert et al. 1999; Kossin and Schubert 2001). Signals characterizing the ring of maximum winds (RMW_{AZ} and $Vmax_{AZ}$), on the other hand, do not appear in these 10 best combinations.

More generally, the scores associated with these 10 combinations range between 63% and almost 65%. In comparison, the score associated with the combination of vortex-averaged parameters (i.e., latitude, RMW, V_{MAX}, and dV/dR_{EW}), featured by the horizontal black line in Fig. 11), is 60%, and the score of the worst combination is around 43%. Note again here that the method is not designed to bring the best possible prediction score (because a limited number of variable is used in

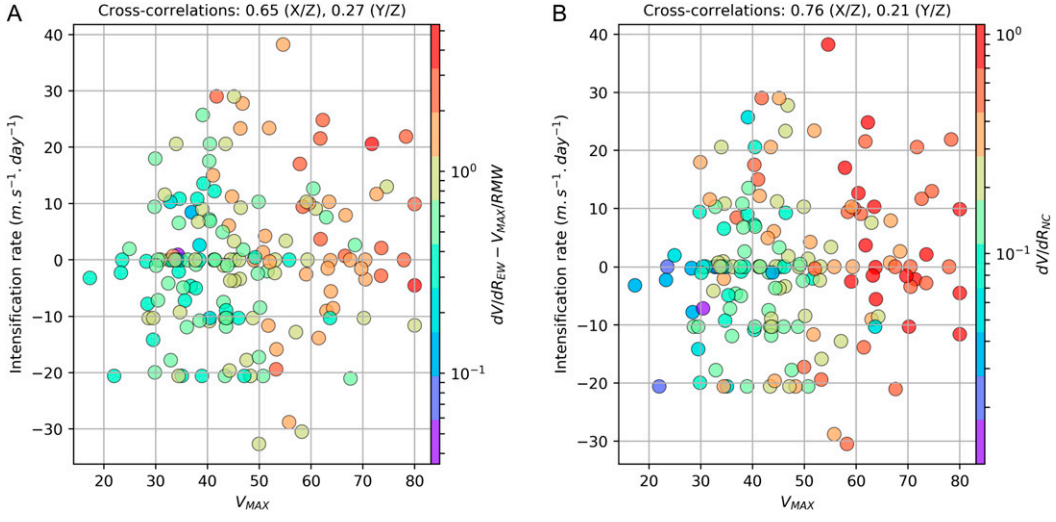

FIG. 9. Distribution as a function of maximum wind (x axis) and intensification rate (y axis) of (a) eyewall wind gradient in comparison with Rankine vortex ($dV/dR_{EW} - V_{MAX}/RMW$; $m\,s^{-1}\,km^{-1}$) and (b) near-core radial gradient (dV/dR_{NC}; $m\,s^{-1}\,km^{-1}$). Titles indicate the cross correlations between radial gradients and both intensity (X/Z) and intensification rate (Y/Z).

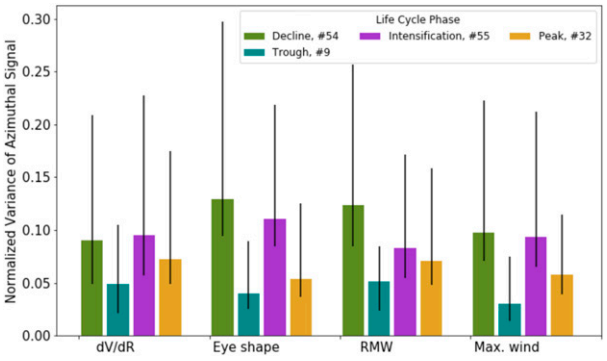

FIG. 10. Normalized variance of the four azimuthal signals (dV/dR, eye shape, RMW, and V_{MAX}) for four life-cycle phases: stable intensification (purple), stable decline (green), intensity peak (yellow), and intensity trough (cyan). Bars and error bars respectively denote the median and the quartiles.

each combination) but rather to assess the potential contribution of our SAR-extracted parameters. In addition, while these score variations might seem small, they can be considered as true indicators of an improvement in the classification as they are averaged over 10 models, performing bootstrap methods for each model, and iterated 10 times each with a different random control variable, ensuring to take into account the variability associated with the machine-learning approach.

The prevalence of high wavenumbers describing ES_{AZ} and dV/dR_{AZ}, the two signals estimated in the eyewall area (while RMW_{AZ} and $Vmax_{AZ}$ describe the maximum wind ring), indicates a contribution of inner-core internal dynamics to the classification. Indeed, these wavenumbers correspond to small-scale dynamic processes: eyewall processes such as convective bursts and mesovortices, for instance, sign on such small scales (Schubert et al. 1999; Kossin and Schubert 2001), while smaller wavenumbers represent a more general measure of asymmetry at the vortex scale. It can also be noted that the lowest score is associated with combinations containing dV/dR_{AZ} wavenumbers 1 and 2 (these lowest combinations are not shown on the figure). Thus, a true scale separation occurs between this vortex scale and the smaller scale describing localized structures in the eyewall.

We thus show with this machine-learning approach that eyewall small-scale dynamics (characterized through the eye shape and eyewall radial gradient spectral decomposition) has the potential to improve a statistical prediction of TC intensity variations relative to the sole use of vortex-averaged parameters and synoptic information.

4. Summary and discussion

In this study, we have analyzed 188 high-resolution (1 km) SAR images of TCs. In addition to their outstanding resolution, these images present the advantage of having a large spatial extent allowing for a characterization of the whole 2D TC wind structure at the sea surface. The wind retrieval is performed using the dual-polarization capacity of Sentinel-1 and *RADARSAT-2* SARs, which has been shown to faithfully retrieve TC high wind speeds (Mouche et al. 2017). Taking advantage of this newly available dataset, which contains at least 15 images for each TC intensity category, our study demonstrates the ability to describe and characterize, with such acquisitions, the TC inner core, through its radial profile, its azimuthal degree of asymmetry, and the energy distribution in the eyewall and maximum wind areas.

a. SAR observations and TC internal dynamics

The statistical analysis evidences a TC size reduction, and a sharpening of the eyewall radial wind profile with intensity, consistent with previous studies (Shea and Gray 1973; Shapiro and Willoughby 1982; Willoughby et al. 1982; Willoughby 1990).

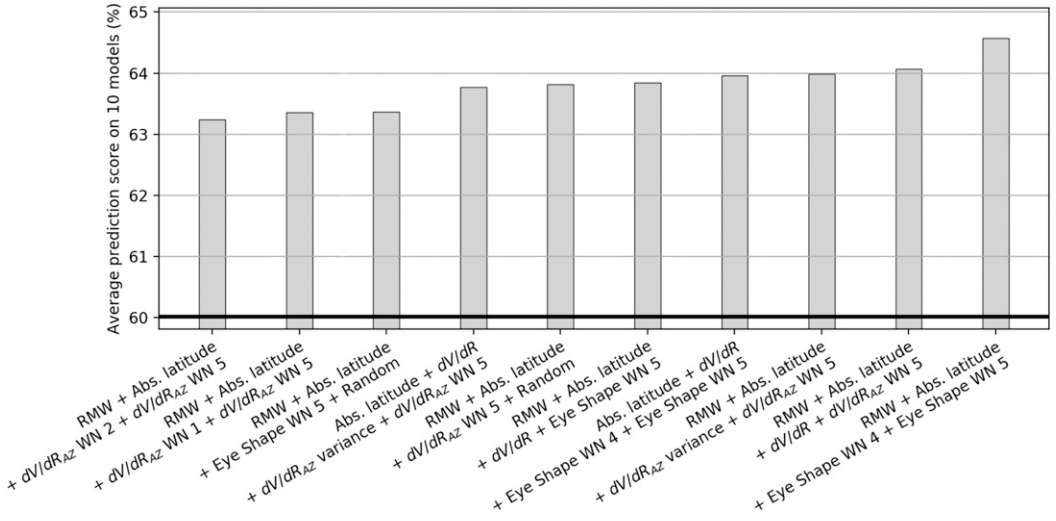

FIG. 11. Average prediction scores (%) obtained over 10 machine-learning models for the 10 best random combinations of four SAR-extracted parameters. The x axis features the variables composing each combination. The black horizontal line denotes the score obtained for the combination containing only mean vortex-averaged parameters (latitude, V_{MAX}, RMW, and dV/dR_{EW}).

Willoughby et al. (1982), Willoughby (1990), and Schubert and Hack (1982) described TC contraction as resulting from the increased wind gradient in the inner edge of the maximum wind area (this increased gradient itself associated with latent heat release and isobaric height fall in the inner side of the convective ring). Studies by Schubert et al. (1999), Kossin and Eastin (2001), and Nguyen et al. (2011) further discussed the role played by mesovortices generated in the eyewall inner edge, which induce mixing and consequently spinup within the eye, and then increased convective available potential energy in the vicinity of the ring of maximum winds when these mesovortices dissipate and move outwards as VRWs. During this process, the vortex transitions from U-shape to a Rankine-like vortex, and back to a U-shape vortex. Our observations support these previous results. We show a variety of observed wind profiles and shapes, even at high intensity. In average, a relationship between eyewall gradients and both intensity and intensification rates is evidenced, and inner-core wind gradients are shown to increase superlinearly with intensity, as illustrated by the gradually increased departure from the likely solid-body rotation profile. Such sharper gradients may also be seen as a consequence of the BL spinup process (Smith et al. 2008; Bryan and Rotunno 2009), as supergradient winds near the RMW would increase the radial gradient. This process, supposed to increase with intensity (Stern and Nolan 2011), could explain the increased departure from the solid-body rotation that we observe. In a recent analytical model development, Chavas et al. (2015) proposed to adjust their inner-core profile toward a slightly superlinear solution to avoid an overestimation of the wind in the eye, and better fit observations. Our results suggest that such an adjustment should depend on TC intensity, and that SAR observations could help further constraining TC parametric wind models.

The near-core wind gradient profile (computed from RMW to 3 RMW) is also of interest, as it characterizes the broadness of the azimuthal-mean wind peak, and the decay rate of the outer profile, which are useful for risk assessment (Croxford and Barnes 2002) and related to the vortex resiliency to external shear (Reasor et al. 2004). The analysis of Mallen et al. (2005), from flight-level aircraft observations, linked the vortex resiliency to the near-core profile shapes. Our analysis of near-core gradients, showing on average their superlinear increase with intensity, seems to indicate in this context that stronger TCs (especially above category 4) are comparatively less resilient to wind shear, as their sharper profile is more likely to cause a radial distribution of potential vorticity favorable to tilt instability (Reasor et al. 2004). Further analyses could certainly help in evaluating the primary circulation broadness and subsequent vortex resiliency to shear events, possibly providing new guidance for TC forecasters.

Our analyses also revealed a lower sensitivity of the near-core gradient to the intensification rate relative to the eyewall gradient, suggesting a partial decoupling between these two areas. The generation of mesovortices in the eyewall area, observed in several of our images, and also discussed in previous studies (Schubert et al. 1999; Nguyen et al. 2011; Li et al. 2013), indicate a very reactive dynamics of the inner eyewall area, therefore, more correlated to intensity variations. The observed decoupling may also advocate for the dual spinup theory proposed by Smith et al. (2009), which suggests that inner-core and outer-core dynamics are monitored by two distinct kinds of spinup, the former occurring in the BL with supergradient winds, and the latter occurring above the BL in classical gradient wind balance.

The investigation of spectral energy distributions in the eyewall and in the maximum wind area further reveals this decoupling. While the azimuthal distribution of the eyewall radial wind gradient shows no notable sensitivity to intensity, the maximum wind contour is found to homogenize (broadening of its energy spectrum toward large wavenumbers) with intensity. In addition, the analysis of both ES_{AZ} and RMW_{AZ} variance shows an axisymmetrization of the TC shape. These two features seem in agreement with the VRWs theory. By propagating energy from the vortex center to its upper and outer boundaries, VRWs act to restore the TC structure from interactions of the main vortex with inner-core mesovortices (Nolan and Montgomery 2002) or external events such as vertical wind shear (Montgomery and Kallenbach 1997), that may prevent TC intensification by tilting the vortex (Reasor et al. 2004). VRWs generate asymmetries in the eyewall and high-wind area (Schubert et al. 1999), causing barotropic instabilities that can limit the TC intensity while reducing the eyewall tilt (Yang et al. 2007). Our analyses show that intense TCs have a more symmetric structure and distributed energy spectrum, indicating less intense VRW activity. The assessment of VRWs propagation from our database is, however, limited by the instantaneous nature of SAR images and the lack of continuity in TC sampling.

Overall, SAR provides unique high-resolution estimates of the ocean surface wind speed, with applications for the study of eyewall dynamics (inner-core BL spinup, mesovortices generation and associated vorticity mixing, and their relationship to intensity changes), vortex strength and resiliency, and intensity restoration processes in the inner core such as VRWs. They allow a statistical characterization of these properties on a relatively large range of cases. Although their temporal sampling limits the analyses to snapshots and surface measurements, SAR acquisitions shall be seen as a complement to other sources for the observation of the TC's internal structure and dynamics.

b. SAR observations and TC life-cycle variations

Our study finally assessed the potential of TC inner-core SAR-extracted parameters (radial profile, azimuthal and energetic distributions) in characterizing the ongoing TC intensity variations in a future perspective of predictability improvement.

We observed sharper eyewall and near-core gradients with both increasing intensity and intensification rate. This indicates a trend toward a U-shape profile, and a reduced broadness of the primary circulation for intensifying TCs. These results are consistent with the modeling studies of Nguyen et al. (2011) and Kossin and Eastin (2001), which found "symmetric" phases of lower mesovortical activity (phase A for Kossin and Eastin 2001) to be more favorable to fast intensifications. The observed increase of the near-core gradient with intensification rate also suggests a reduced broadness of the primary

circulation, and a lower resiliency to external events as suggested by Mallen et al. (2005).

The evolution of TC shape or energetic azimuthal signals with intensification rate and TC life phases reveals that TCs in a transition phase toward reintensification (after a decline phase) are the most symmetric. To further estimate the contribution of all SAR-extracted parameters in TC life-cycle prediction, we designed a machine-learning approach, which classifies intensifying and decaying TC phases. The contribution of the various extracted parameters was then assessed by sorting the prediction scores obtained from different combinations of variables. The best combinations revealed a notable contribution of the eye shape and eyewall wind gradient high wavenumbers (WNs 4 and 5), improving by 4.5% (from 60% to 64.5%) the score obtained with vortex-averaged parameters only.

This improvement highlights the importance of small-scale processes in the prediction of intensity variations. Indeed, wavenumbers 4 and 5 in the eye shape correspond to localized structures with a reduced spatial scale, such as convective asymmetries and rainbands perturbing the eyewall. Judt et al. (2016) referred to wavenumbers 2–5 as the ''rainband scale,'' and Schubert and Hack (1982) modeled a wavenumber 4 disturbance and related it to the formation of mesovortices. These small-scale features may also be linked to the propagation of VRWs (Schubert et al. 1999; Wang 2002a). In the literature, only low wavenumbers (1 and 2) are usually studied (Reasor et al. 2000; Wang 2002b) due to observational limitations (lack of azimuthal resolution from aircraft sampling, lack of spatial resolution for satellite radiometers and scatterometers). Numerical studies suggest that these wavenumbers are the most influential for vortex evolution (Wang 2001, 2002a) as they are directly related to the environmental forcing.

However, rapid intensity variations are still a challenge to forecast, and may be related to these fine-scale dynamics. Our first assessment of the predictability potential of the inner-core fine-scale properties shows that including high-wavenumber signals improves the characterization and classification of intensity changes. Usual operational statistical–dynamical forecast models (DeMaria and Kaplan 1994, 1999; Knaff et al. 2005; Knaff and Sampson 2009) use linear regression techniques to predict intensity changes from large-scale climatological fields (temperature, humidity, maximum potential intensity, shear...), TC intensity, and rate of change at the forecast initial time. Neetu et al. (2017) showed that the most important predictors of these statistical–dynamical models are the intensity and its rate of change. An accurate estimation of both of these parameters is therefore required (and SAR proves useful for TC intensity retrieval), but our classification suggests that including other finer-scale internal structure parameters (in particular the eye shape and eyewall gradient high wavenumbers) might eventually improve this type of statistical forecast, especially on short time scales. Our dataset is limited, though, to a relatively low number of events and a large number of descriptors for a statistical classification. We therefore could not assess the true added value of each extracted parameter, but rather the more-likely best parameters to consider for predicting TC life cycle. In addition, our machine-learning approach was not designed to actually work as an operational statistical forecast model, which would require to include all available parameters including large-scale environmental fields (temperature, humidity, shear, etc.) along with our fine-scale observations to fully assess forecast issues and effectiveness.

c. *SAR observation limitations*

Besides the potential of new high-resolution SAR wind retrievals, they still have several limitations.

Our description of the TC inner core does not include the eye area (but only the eyewall, maximum wind, and near-core areas), while it could be of interest as the eye dynamics and the degree of convection in the eye are closely related to TC intensification (see Emanuel 2018, part 3e). Limitations in the inversion algorithm used for ocean surface wind retrieval from SAR observations acquired in dual-polarizations may arise in the eye region. They are associated with discrepancies between co- and cross-polarization signals due to the low backscatter signal in this area, and the particularly low signal to noise ratio of the cross-polarization. To compensate for those discrepancies, wind values from the European Centre for Medium-Range Weather Forecasts (ECMWF) model are combined with the dual-polarization data (Mouche et al. 2017). However, ECMWF winds may not be perfectly collocated with the observed TC. In such cases, the eye wind retrieval may therefore be polluted by higher wind values from the model in the eye, yielding to overestimated wind values. The eyewall and the surrounding high-wind area are not subject to this limitation, because the weight of the model is almost zero in these areas (the algorithm taking benefit of the dual polarization). This limit of the inversion algorithm prevents us from studying the wind distribution inside the eye. It can be noted that high values of radar backscattered intensities can actually be measured in the eye of a TC (Li et al. 2013). They have been interpreted as a signature of abnormally high rain or wind, or wind sea–swell interaction in the eye. The inversion algorithm might thus not be the only cause of this inconsistency.

The understanding of rain impacts on ocean scenes acquired by SAR systems is a particularly active subject of debate and investigation in the SAR community (Melsheimer et al. 1998; Atlas 1994a,b) and more specifically for TCs (Katsaros et al. 2000; Mouche et al. 2019; Combot et al. 2020). These signatures can significantly impact the wind field, but their characteristics vary a lot depending on rain and wind field properties. Backscattered signal can be affected through modifications of the surface roughness (waves damping by raindrop-induced turbulence in the water or increased roughness by rain droplets impinging the surface) or contributions from the atmosphere (attenuation and scattering from hydrometeors).

The result on the wind field can take several forms. The most common is an underestimation of the wind speed surrounding the maximum wind area, where the rains are the heaviest. This ''eyebrows-like'' signature is typical of major TCs [see Mouche et al. (2019) or the example of TC Lionrock in Fig. 3a]. These signatures are, however, usually located outward from the ring of maximum wind (Figs. 3a,b), and have a small radial extent. Their impact on the retrieved inner-core signals is thus very limited and no impacted case was identified. On the contrary,

for weaker TCs or in outer rainbands, one can have overestimation of the wind speed (see the example shown in Fig. S1f in the online supplemental material). Such cases may impact our estimates of the maximum wind speed distribution and radial gradients, but they are very rare (only 2 were identified in our dataset).

Moreover, these individual impacts were either attenuated or removed by our preliminary smoothing and masking steps, and by the definition of vortex-averaged and integrated variables such as azimuthal variances and radial mean gradients. They are thus assumed to not noticeably impact our statistical analysis. The study of rain impact on SAR wind retrieval is still, however, a question to be addressed. To date, this field of research still lacks coincident high-resolution measurements of wind and rain collocated with SAR data to fully quantify the rain impact on a statistical basis and yield a more reliable wind inversion algorithm.

Overall, the use of SAR acquisitions in dual-polarization is recent and further work is certainly required to improve the signal quality (especially in cross-polarization and at subswath limits), the relationship between ocean surface wind and backscattered intensity, the possible rain and waves signatures that can coexist, the wind direction estimation, and more generally, the inversion scheme.

Another limiting factor of our study concerns the intensity variation assessment is the absence of temporal continuity in SAR acquisitions. This prevents an estimate of the short-range changes in the internal structure, and of the dynamics of extracted small-scale properties directly from the SAR data. In this study, the temporal variation of TC along with its life cycle is thus given by the BT data. Linear interpolation is performed to align in time the two sources of data, but this does not prevent inconsistency between the two datasets and may degrade the relationship between the SAR-derived parameters and TC intensity variations.

The recently published SATCON database (Velden and Herndon 2020) provides hourly TC intensity estimates based on a combination of infrared and microwave satellite measurements with an objective algorithm. Such a dataset could allow further analysis of the relationship between TC temporal variability and SAR small-scale variability within short intervals to possibly evaluate the benefit of this complementary temporal information for TC intensity variation predictability. Such an objective would require a prior in-depth validation of wind estimates from the two data sources, and thus a dedicated study which is beyond the scope of this paper.

Our dataset, although it is very consistent and covering all TC categories, is still insufficient to fully describe the TC evolution. Additional observations would certainly allow one to refine the characterization of life-cycle phases and strengthen the statistical analyses.

5. Conclusions

The present work aimed at describing the internal structure of TCs as observed from SAR imagery, and at evaluating relationships between this structure and the TC life cycle. It took advantage of acquisitions performed with two satellite SARs (Sentinel-1 and *RADARSAT-2*), which were targeting TC events. These two instruments are C-band SARs operating in both co- and cross-polarization modes, which have been shown to complement one another in retrieving high wind speeds (Mouche et al. 2017), particularly as the cross-polarization implemented on both Sentinel-1 and *RARDARSAT-2* is much more sensitive to high wind gradients. Other SAR missions such as *Advanced Land Observing Satellite 2* (*ALOS-2*), *TerraSAR-X*, or *Gaofen-3* that are currently operating, do not provide, to our knowledge, the facilities and supporting programs to order TC acquisitions on short notice (which is a constrain due to relatively short time range in TC forecast), but could contribute to the TC monitoring at high resolution. Several space agencies also plan the launch of other SAR missions in the coming years [e.g., Sentinel-1 Next-Generation and Radar Observation System for Europe in L-band (ROSE-L) at ESA, ALOS-3 at JAXA, and NASA–Indian Space Research Organisation (ISRO) SAR (NISAR)], and the TC community would certainly benefit from them, if TC monitoring could become one of their targeted applications. Some of these missions are using SAR operated in other acquisition bands (L band or X band). This would require additional research to develop robust high-wind retrieval algorithms but could also bring new insights for radar image interpretation, certainly contributing to improve our understanding of the various components impacting the imaging mechanisms.

Our study shows how its large coverage, together with its ability to measure the sea surface at a very high resolution, makes SAR very valuable for TC research, as well as for operational applications and risk assessment. This urges the need for moving toward an operational SAR acquisition strategy, and for further developments on wind retrieval algorithm over TCs.

The interpretations and results provided in the present study reveal the importance of radial resolution for the description of the eyewall and near-core areas, with possible implications for the understanding of TC intensity fluctuations and future improvement of parametric vortex models such as the one developed by Chavas et al. (2015), as SAR-extracted statistical properties (notably the relationship between inner eyewall profile and maximum wind) could be used to fit and improve existing idealized radial profiles. They also highlight links between TC asymmetry, size and intensity, and the importance of azimuthal resolution in resolving high wavenumbers to improve our ability to dissociate intensification phases. Including some of the SAR-extracted parameters (in particular the eye shape and eyewall gradient high wavenumbers) into statistical forecast models may have a potential of predictability improvement. The statistical analysis of intensity variations could also be refined by extracting smaller-scale parameters such as the properties of BL rolls (i.e., their size, wavelength, amount…). Recent attempts to measure these properties from SAR data are promising (Foster 2005; Huang et al. 2018) and could help characterize the distribution of the convection in the BL. The inclusion of such features in the present statistical dataset could certainly provide further insights on the links between TC life cycle and convection in the BL.

Future work will focus on dynamical models to include the temporal evolution of TC small-scale structure and relate it to intensity changes. Analysis of future SAR observations will also continue to improve our understanding of this new measurement technique and further assess its potential.

Acknowledgments. The SAR database was obtained from IFREMER/CyclObs and produced with the SAR wind processor codeveloped by IFREMER and CLS. The authors also acknowledge the Pôle de Calcul et de Données Marines (PCDM) for providing DATARMOR storage and computational resources (http://www.ifremer.fr/pcdm). This work was supported by the French National Institute for Ocean Science (IFREMER), the Institute for Research and Development (IRD), and by the French national programme LEFE/INSU. The paper benefited from the comments provided by two reviewers.

Data availability statement. The SAR TC images dataset used in this study is available online (https://cyclobs.ifremer.fr/).

APPENDIX

Details on SAR Image Processing

The following sections detail the procedures of image processing mentioned in section 2c and shown in Fig. 2.

a. Masking: Subswaths, outliers, and rain signatures

First, we address subswaths and outliers: Subswath signatures can be identified in the SAR wind speed retrievals, indicating that wind values in their vicinity are probably erroneous. We therefore detect these subswath signatures based on their high value of column-wise average wind gradient, and mask them (Fig. 2a, blue lines). Subswaths and issues with the acquisition can sometimes cause larger signatures in the wind field, for which this filtering step may not be sufficient, but it overall removes most of the subswath signatures, which could hamper our azimuthal signals extraction. A second masking procedure is applied consisting of a pixel-wise mask to remove any pixel outlier (e.g., spike pixel values in the wind field not corresponding to a realistic wind structure).

We then turn to heterogeneity mask and rain signatures. The SAR wind product additionally includes a heterogeneity mask designed to remove non-wind-related features associated with high local gradient values (Fig. 2a, gray contours). Such structures are often due to heavy rain impacting the SAR NRCS signal. Rain impact on SAR measurements is indeed a preoccupying feature of SAR inversion algorithms. Mouche et al. (2019) showed, in the case of Hurricane Irma, that heavy rain can either attenuate or enhance the NRCS signal but concluded that "at this stage, there is not enough evidence to conclude if these overall signal changes are solely due to rain impacts, to wind changes, or to their combined effects." Combot et al. (2020) also conducted a statistical assessment of rain impact on the SAR estimation of V_{MAX} and RMW using rain-rate estimates inferred from IMERG product collocated with SAR acquisitions in time and space (±10 km around the SAR-derived RMW). They showed that V_{MAX} SAR estimates can be significantly affected by rain, whereas RMW is less sensitive.

Automated removal of rain artifacts is, however, very difficult, and in-depth dedicated research is requested to address this issue. The heterogeneity mask, used in the present study, removes part of the rain-induced artifacts of the SAR wind field, and remaining rain artifacts are considered to not significantly impact our analyses. Indeed, visual inspection of several case studies has shown that remaining rain signatures are mostly external to the maximum wind ring, and additionally the smoothing step applied on our extracted signals, and the statistical analyses performed on numerous cases limit the impact of local anomalies in SAR wind fields. A complementary discussion of rain impacts is provided in section 4c.

b. Locating the TC center

The second step of SAR image processing is to detect the TC center. Indeed, even though the TC center derived from BT has been interpolated, it is not always collocated with the center of the TC eye, as illustrated in Fig. 2a. The step of TC-center positioning is crucial for our study because all TC properties are then described in a polar grid referenced on the TC center. Its retrieval is designed to be generic and automatic, working on level-2 data. The procedure consists of the following steps and is illustrated in Fig. 2 for a Sentinel-1 SAR acquisition performed on 27 August 2016 on TC Lionrock (western Pacific).

Because the TC eye is a region of strong wind gradient, it is often partially masked by the heterogeneity mask described in the previous paragraph (see gray contours in Fig. 2a). For this step of TC-center research, we thus temporarily remove the heterogeneity mask around the BT interpolated TC center, in a radius defined as the maximum between $4RMW_{BT}$ and $R34_{BT}$ (Fig. 2a, black dashed line). The heterogeneity mask is later reapplied on the polar-projected data out of $1.5 \times RMW_{SAR}$.

Several TC-center extraction algorithms have been developed for SAR images. Most of them rely on a wavelet analysis of the level-1 surface roughness images to find the TC center (Zheng et al. 2017). In the present study, as we use level-2 wind speed data, a new method is designed based on several wind speed thresholds to gradually approach the TC center. First, the pixels corresponding to the highest wind speed values, defined as the upper 80% of the wind range in a radius defined as the maximum between $2RMW_{BT}$ and $R34_{BT}/2$ around the BT center (Figs. 2a,b, red dashed line), are identified (Fig. 2b, red contour), and their centroid is located (magenta dot). Then, in a similar way, the centroid (cyan dot) of the low-wind area (lower 20% of the wind speed range, gray contour) in a radius of $2RMW_{BT}$ around the high-wind centroid (magenta dashed line) is located. This low-wind centroid is then iteratively recomputed, in a radius of $2RMW_{BT}$ around the last estimated low-wind centroid to ensure finding a stable location. Indeed, in some cases, the first low-wind centroid guess might fall outside the eye, in the high-wind vicinity. In such cases, the iterative procedure locates the centroid farther from the high-wind area and no stability is found. If so, the low-wind centroid research is reprocessed within a smaller radius of research

around the high-wind centroid until finding a stable low-wind centroid. This procedure manages to find the TC center in a vast majority of cases, although some exceptions can occur. To prevent errors in the polar projection in cases in which the low-wind centroid is offset with respect to the vortex structure (mostly when the eye is large and distorted or when the wind distribution in the eye is not uniform), a recentering step is carried out. This last step consists in locating the centroid (yellow dot) of the eye shape, defined as the maximal radial wind gradient for each azimuth (black line in Fig. 2b) around the low-wind centroid. In cases in which the eye-shape centroid falls outside the polygon (when the eye is distorted and the polygon is concave), the final TC center is defined as the pole of inaccessibility of the polygon, i.e., the "most distant internal point from the polygon outline." The final TC center is thus defined as the eye-shape polygon centroid (or pole of inaccessibility in concave eye configuration).

REFERENCES

Atlas, D., 1994a: Footprints of storms on the sea: A view from spaceborne synthetic aperture radar. *J. Geophys. Res.*, **99**, 7961–7969, https://doi.org/10.1029/94JC00250.

——, 1994b: Origin of storm footprints on the sea seen by synthetic aperture radar. *Science*, **266**, 1364–1366, https://doi.org/10.1126/science.266.5189.1364.

Bender, M. A., and I. Ginis, 2000: Real-case simulations of hurricane–ocean interaction using a high-resolution coupled model: Effects on hurricane intensity. *Mon. Wea. Rev.*, **128**, 917–946, https://doi.org/10.1175/1520-0493(2000)128<0917:RCSOHO>2.0.CO;2.

Bryan, G. H., and R. Rotunno, 2009: Evaluation of an analytical model for the maximum intensity of tropical cyclones. *J. Atmos. Sci.*, **66**, 3042–3060, https://doi.org/10.1175/2009JAS3038.1.

Cangialosi, J. P., and J. Franklin, 2019: National Hurricane Center forecast verification report. NOAA National Hurricane Center Tech. Rep., 82 pp., http://www.nhc.noaa.gov/verification/pdfs/Verification_2014.pdf.

Charney, J. G., and A. Eliassen, 1964: On the growth of the hurricane depression. *J. Atmos. Sci.*, **21**, 68–75, https://doi.org/10.1175/1520-0469(1964)021<0068:OTGOTH>2.0.CO;2.

Chavas, D. R., N. Lin, and K. Emanuel, 2015: A model for the complete radial structure of the tropical cyclone wind field. Part I: Comparison with observed structure. *J. Atmos. Sci.*, **72**, 3647–3662, https://doi.org/10.1175/JAS-D-15-0014.1.

Chen, Y., and M. Yau, 2001: Spiral bands in a simulated hurricane. Part I: Vortex Rossby wave verification. *J. Atmos. Sci.*, **58**, 2128–2145, https://doi.org/10.1175/1520-0469(2001)058<2128:SBIASH>2.0.CO;2.

Combot, C., A. Mouche, J. Knaff, Y. Zhao, Y. Zhao, L. Vinour, Y. Quilfen, and B. Chapron, 2020: Extensive high-resolution synthetic aperture radar (SAR) data analysis of tropical cyclones: Comparisons with SFMR flights and best track. *Mon. Wea. Rev.*, **148**, 4545–4563, https://doi.org/10.1175/MWR-D-20-0005.1.

Corbosiero, K. L., J. Molinari, A. R. Aiyyer, and M. L. Black, 2006: The structure and evolution of Hurricane Elena (1985). Part II: Convective asymmetries and evidence for vortex Rossby waves. *Mon. Wea. Rev.*, **134**, 3073–3091, https://doi.org/10.1175/MWR3250.1.

Croxford, M., and G. M. Barnes, 2002: Inner core strength of Atlantic tropical cyclones. *Mon. Wea. Rev.*, **130**, 127–139, https://doi.org/10.1175/1520-0493(2002)130<0127:ICSOAT>2.0.CO;2.

DeMaria, M., and J. Kaplan, 1994: A Statistical Hurricane Intensity Prediction Scheme (SHIPS) for the Atlantic basin. *Wea. Forecasting*, **9**, 209–220, https://doi.org/10.1175/1520-0434(1994)009<0209:ASHIPS>2.0.CO;2.

——, and ——, 1999: An updated Statistical Hurricane Intensity Prediction Scheme (SHIPS) for the Atlantic and eastern North Pacific basins. *Wea. Forecasting*, **14**, 326–337, https://doi.org/10.1175/1520-0434(1999)014<0326:AUSHIP>2.0.CO;2.

Du, Y., and P. W. Vachon, 2003: Characterization of hurricane eyes in RADARSAT-1 images with wavelet analysis. *Can. J. Remote Sens.*, **29**, 491–498, https://doi.org/10.5589/m03-020.

Dvorak, V. F., 1975: Tropical cyclone intensity analysis and forecasting from satellite imagery. *Mon. Wea. Rev.*, **103**, 420–430, https://doi.org/10.1175/1520-0493(1975)103<0420:TCIAAF>2.0.CO;2.

Elsberry, R. L., L. Chen, J. Davidson, R. Rogers, Y. Wang, and L. Wu, 2013: Advances in understanding and forecasting rapidly changing phenomena in tropical cyclones. *Trop. Cyclone Res. Rev.*, **2**, 13–24, https://doi.org/10.6057/2013TCRR01.02.

Emanuel, K. A., 1986: An air–sea interaction theory for tropical cyclones. Part I: Steady-state maintenance. *J. Atmos. Sci.*, **43**, 585–605, https://doi.org/10.1175/1520-0469(1986)043<0585:AASITF>2.0.CO;2.

——, 1987: The dependence of hurricane intensity on climate. *Nature*, **326**, 483–485, https://doi.org/10.1038/326483a0.

——, 2018: 100 years of progress in tropical cyclone research. *A Century of Progress in Atmospheric and Related Sciences*, *Meteor. Monogr.*, No. 59, Amer. Meteor. Soc., https://doi.org/10.1175/AMSMONOGRAPHS-D-18-0016.1.

Foster, R. C., 2005: Why rolls are prevalent in the hurricane boundary layer. *J. Atmos. Sci.*, **62**, 2647–2661, https://doi.org/10.1175/JAS3475.1.

Franklin, J. L., S. J. Lord, and F. D. Marks Jr., 1988: Dropwindsonde and radar observations of the eye of Hurricane Gloria (1985). *Mon. Wea. Rev.*, **116**, 1237–1244, https://doi.org/10.1175/1520-0493(1988)116<1237:DAROOT>2.0.CO;2.

Friedman, K. S., and X. Li, 2000: Monitoring hurricanes over the ocean with wide swath SAR. *Johns Hopkins APL Tech. Dig.*, **21**, 80–85.

Holland, G. J., J. I. Belanger, and A. Fritz, 2010: A revised model for radial profiles of hurricane winds. *Mon. Wea. Rev.*, **138**, 4393–4401, https://doi.org/10.1175/2010MWR3317.1.

Houze, R. A., Jr., S. S. Chen, B. F. Smull, W.-C. Lee, and M. M. Bell, 2007: Hurricane intensity and eyewall replacement. *Science*, **315**, 1235–1239, https://doi.org/10.1126/science.1135650.

Huang, L., X. Li, B. Liu, J. A. Zhang, D. Shen, Z. Zhang, and W. Yu, 2018: Tropical cyclone boundary layer rolls in synthetic aperture radar imagery. *J. Geophys. Res. Oceans*, **123**, 2981–2996, https://doi.org/10.1029/2018JC013755.

Jin, S., S. Wang, and X. Li, 2014: Typhoon eye extraction with an automatic SAR image segmentation method. *Int. J. Remote Sens.*, **35**, 3978–3993, https://doi.org/10.1080/01431161.2014.916447.

——, ——, ——, L. Jiao, and J. A. Zhang, 2017: Tropical cyclone center location in SAR images based on feature learning and visual saliency. *Hurricane Monitoring with Spaceborne Synthetic Aperture Radar*, Springer, 141–181.

Jordan, C. L., 1961: Marked changes in the characteristics of the eye of intense typhoons between the deepening and filling stages. *J. Meteor.*, **18**, 779–789, https://doi.org/10.1175/1520-0469(1961)018<0779:MCITCO>2.0.CO;2.

Judt, F., S. S. Chen, and J. Berner, 2016: Predictability of tropical cyclone intensity: Scale-dependent forecast error growth in high-resolution stochastic kinetic-energy backscatter

ensembles. *Quart. J. Roy. Meteor. Soc.*, **142**, 43–57, https://doi.org/10.1002/qj.2626.

Jullien, S., P. Marchesiello, C. E. Menkes, J. Lefèvre, N. C. Jourdain, G. Samson, and M. Lengaigne, 2014: Ocean feedback to tropical cyclones: Climatology and processes. *Climate Dyn.*, **43**, 2831–2854, https://doi.org/10.1007/s00382-014-2096-6.

Katsaros, K. B., P. W. Vachon, P. G. Black, P. P. Dodge, and E. W. Uhlhorn, 2000: Wind fields from SAR: Could they improve our understanding of storm dynamics? *Johns Hopkins APL Tech. Dig.*, **21**, 86–93, https://doi.org/10.4095/219617.

——, ——, W. T. Liu, and P. G. Black, 2002: Microwave remote sensing of tropical cyclones from space. *J. Oceanogr.*, **58**, 137–151, https://doi.org/10.1023/A:1015884903180.

Knaff, J. A., and C. R. Sampson, 2009: Southern Hemisphere tropical cyclone intensity forecast methods used at the Joint Typhoon Warning Center, part II: Statistical–dynamical forecasts. *Aust. Meteor. Oceanogr. J.*, **58**, 9–18, https://doi.org/10.22499/2.5801.002.

——, ——, and M. DeMaria, 2005: An operational Statistical Typhoon Intensity Prediction Scheme for the western North Pacific. *Wea. Forecasting*, **20**, 688–699, https://doi.org/10.1175/WAF863.1.

Knapp, K. R., M. C. Kruk, D. H. Levinson, H. J. Diamond, and C. J. Neumann, 2010: The International Best Track Archive for Climate Stewardship (IBTrACS) unifying tropical cyclone data. *Bull. Amer. Meteor. Soc.*, **91**, 363–376, https://doi.org/10.1175/2009BAMS2755.1.

Kossin, J. P., and M. D. Eastin, 2001: Two distinct regimes in the kinematic and thermodynamic structure of the hurricane eye and eyewall. *J. Atmos. Sci.*, **58**, 1079–1090, https://doi.org/10.1175/1520-0469(2001)058<1079:TDRITK>2.0.CO;2.

——, and W. H. Schubert, 2001: Mesovortices, polygonal flow patterns, and rapid pressure falls in hurricane-like vortices. *J. Atmos. Sci.*, **58**, 2196–2209, https://doi.org/10.1175/1520-0469(2001)058<2196:MPFPAR>2.0.CO;2.

Kuo, H.-C., R. Williams, and J.-H. Chen, 1999: A possible mechanism for the eye rotation of Typhoon Herb. *J. Atmos. Sci.*, **56**, 1659–1673, https://doi.org/10.1175/1520-0469(1999)056<1659:APMFTE>2.0.CO;2.

Lee, I. K., A. Shamsoddini, X. Li, J. C. Trinder, and Z. Li, 2016: Extracting hurricane eye morphology from spaceborne SAR images using morphological analysis. *ISPRS J. Photogramm. Remote Sens.*, **117**, 115–125, https://doi.org/10.1016/j.isprsjprs.2016.03.020.

Lee, W.-C., and M. M. Bell, 2007: Rapid intensification, eyewall contraction, and breakdown of Hurricane Charley (2004) near landfall. *Geophys. Res. Lett.*, **34**, L02802, https://doi.org/10.1029/2006GL027889.

Li, X., J. A. Zhang, X. Yang, W. G. Pichel, M. DeMaria, D. Long, and Z. Li, 2013: Tropical cyclone morphology from spaceborne synthetic aperture radar. *Bull. Amer. Meteor. Soc.*, **94**, 215–230, https://doi.org/10.1175/BAMS-D-11-00211.1.

Liu, A. K., S. He, Y. Pan, and J. Yang, 2014: Observations of typhoon eye using SAR and IR sensors. *Int. J. Remote Sens.*, **35**, 3966–3977, https://doi.org/10.1080/01431161.2014.916450.

Long, D., and C. Nie, 2017: Hurricane precipitation observed by SAR. *Hurricane Monitoring with Spaceborne Synthetic Aperture Radar*, Springer, 1–24.

Macdonald, N. J., 1968: The evidence for the existence of Rossby-like waves in the hurricane vortex. *Tellus*, **20**, 138–150, https://doi.org/10.3402/tellusa.v20i1.9993.

Mallen, K. J., M. T. Montgomery, and B. Wang, 2005: Reexamining the near-core radial structure of the tropical cyclone primary circulation: Implications for vortex resiliency. *J. Atmos. Sci.*, **62**, 408–425, https://doi.org/10.1175/JAS-3377.1.

Marks, F. D., 2003: State of the science: Radar view of tropical cyclones. *Radar and Atmospheric Science: A Collection of Essays in Honor of David Atlas*, Springer, 33–74.

Meissner, T., and F. J. Wentz, 2009: Wind-vector retrievals under rain with passive satellite microwave radiometers. *IEEE Trans. Geosci. Remote Sens.*, **47**, 3065–3083, https://doi.org/10.1109/TGRS.2009.2027012.

Melsheimer, C., W. Alpers, and M. Gade, 1998: Investigation of multifrequency/multipolarization radar signatures of rain cells over the ocean using SIR-C/X-SAR data. *J. Geophys. Res.*, **103**, 18 867–18 884, https://doi.org/10.1029/98JC00779.

Miller, B. I., 1958: On the maximum intensity of hurricanes. *J. Meteor.*, **15**, 184–195, https://doi.org/10.1175/1520-0469(1958)015%3C0184:OTMIOH%3E2.0.CO;2.

Miller, R. J., A. J. Schrader, C. R. Sampson, and T. L. Tsui, 1990: The Automated Tropical Cyclone Forecasting System (ATCF). *Wea. Forecasting*, **5**, 653–660, https://doi.org/10.1175/1520-0434(1990)005<0653:TATCFS>2.0.CO;2.

Montgomery, M. T., and R. J. Kallenbach, 1997: A theory for vortex Rossby-waves and its application to spiral bands and intensity changes in hurricanes. *Quart. J. Roy. Meteor. Soc.*, **123**, 435–465, https://doi.org/10.1002/qj.49712353810.

——, and R. K. Smith, 2014: Paradigms for tropical cyclone intensification. *Aust. Meteor. Oceanogr. J.*, **64**, 37–66.

Mouche, A. A., B. Chapron, B. Zhang, and R. Husson, 2017: Combined co- and cross-polarized SAR measurements under extreme wind conditions. *IEEE Trans. Geosci. Remote Sens.*, **55**, 6746–6755, https://doi.org/10.1109/TGRS.2017.2732508.

——, ——, J. Knaff, Y. Zhao, B. Zhang, and C. Combot, 2019: Copolarized and cross-polarized SAR measurements for high-resolution description of major hurricane wind structures: Application to IRMA category 5 hurricane. *J. Geophys. Res. Oceans*, **124**, 3905–3922, https://doi.org/10.1029/2019JC015056.

Muramatsu, T., 1986: The structure of polygonal eye of a typhoon. *J. Meteor. Soc. Japan*, **64**, 913–921, https://doi.org/10.2151/jmsj1965.64.6_913.

Neetu, S., and Coauthors, 2017: Global assessment of tropical cyclone intensity statistical–dynamical hindcasts. *Quart. J. Roy. Meteor. Soc.*, **143**, 2143–2156, https://doi.org/10.1002/qj.3073.

Nguyen, M. C., M. J. Reeder, N. E. Davidson, R. K. Smith, and M. T. Montgomery, 2011: Inner-core vacillation cycles during the intensification of Hurricane Katrina. *Quart. J. Roy. Meteor. Soc.*, **137**, 829–844, https://doi.org/10.1002/qj.823.

Nolan, D. S., and M. T. Montgomery, 2002: Nonhydrostatic, three-dimensional perturbations to balanced, hurricane-like vortices. Part I: Linearized formulation, stability, and evolution. *J. Atmos. Sci.*, **59**, 2989–3020, https://doi.org/10.1175/1520-0469(2002)059<2989:NTDPTB>2.0.CO;2.

Olander, T. L., and C. S. Velden, 2007: The advanced Dvorak technique: Continued development of an objective scheme to estimate tropical cyclone intensity using geostationary infrared satellite imagery. *Wea. Forecasting*, **22**, 287–298, https://doi.org/10.1175/WAF975.1.

Ooyama, K., 1964: A dynamical model for the study of tropical cyclone development. *Geofis. Int.*, **4**, 187–198, https://ci.nii.ac.jp/naid/10003556859/en/.

——, 1969: Numerical simulation of the life cycle of tropical cyclones. *J. Atmos. Sci.*, **26**, 3–40, https://doi.org/10.1175/1520-0469(1969)026<0003:NSOTLC>2.0.CO;2.

Reasor, P. D., M. T. Montgomery, F. D. Marks Jr., and J. F. Gamache, 2000: Low-wavenumber structure and evolution of the hurricane inner core observed by airborne dual-Doppler

radar. *Mon. Wea. Rev.*, **128**, 1653–1680, https://doi.org/10.1175/1520-0493(2000)128<1653:LWSAEO>2.0.CO;2.

——, ——, and L. D. Grasso, 2004: A new look at the problem of tropical cyclones in vertical shear flow: Vortex resiliency. *J. Atmos. Sci.*, **61**, 3–22, https://doi.org/10.1175/1520-0469(2004)061<0003:ANLATP>2.0.CO;2.

Reul, N., and Coauthors, 2017: A new generation of tropical cyclone size measurements from space. *Bull. Amer. Meteor. Soc.*, **98**, 2367–2385, https://doi.org/10.1175/BAMS-D-15-00291.1.

Schubert, W. H., and J. J. Hack, 1982: Inertial stability and tropical cyclone development. *J. Atmos. Sci.*, **39**, 1687–1697, https://doi.org/10.1175/1520-0469(1982)039<1687:ISATCD>2.0.CO;2.

——, M. T. Montgomery, R. K. Taft, T. A. Guinn, S. R. Fulton, J. P. Kossin, and J. P. Edwards, 1999: Polygonal eyewalls, asymmetric eye contraction, and potential vorticity mixing in hurricanes. *J. Atmos. Sci.*, **56**, 1197–1223, https://doi.org/10.1175/1520-0469(1999)056<1197:PEAECA>2.0.CO;2.

Shapiro, L. J., and H. E. Willoughby, 1982: The response of balanced hurricanes to local sources of heat and momentum. *J. Atmos. Sci.*, **39**, 378–394, https://doi.org/10.1175/1520-0469(1982)039<0378:TROBHT>2.0.CO;2.

Shea, D. J., and W. M. Gray, 1973: The hurricane's inner core region. I. Symmetric and asymmetric structure. *J. Atmos. Sci.*, **30**, 1544–1564, https://doi.org/10.1175/1520-0469(1973)030<1544:THICRI>2.0.CO;2.

Smith, R. K., M. T. Montgomery, and S. Vogl, 2008: A critique of Emanuel's hurricane model and potential intensity theory. *Quart. J. Roy. Meteor. Soc.*, **134**, 551–561, https://doi.org/10.1002/qj.241.

——, ——, and N. Van Sang, 2009: Tropical cyclone spin-up revisited. *Quart. J. Roy. Meteor. Soc.*, **135**, 1321–1335, https://doi.org/10.1002/qj.428.

Stern, D. P., and D. S. Nolan, 2011: On the vertical decay rate of the maximum tangential winds in tropical cyclones. *J. Atmos. Sci.*, **68**, 2073–2094, https://doi.org/10.1175/2011JAS3682.1.

——, and F. Zhang, 2013: How does the eye warm? Part I: A potential temperature budget analysis of an idealized tropical cyclone. *J. Atmos. Sci.*, **70**, 73–90, https://doi.org/10.1175/JAS-D-11-0329.1.

——, J. L. Vigh, D. S. Nolan, and F. Zhang, 2015: Revisiting the relationship between eyewall contraction and intensification. *J. Atmos. Sci.*, **72**, 1283–1306, https://doi.org/10.1175/JAS-D-14-0261.1.

Uhlhorn, E. W., B. W. Klotz, T. Vukicevic, P. D. Reasor, and R. F. Rogers, 2014: Observed hurricane wind speed asymmetries and relationships to motion and environmental shear. *Mon. Wea. Rev.*, **142**, 1290–1311, https://doi.org/10.1175/MWR-D-13-00249.1.

Velden, C. S., and D. Herndon, 2020: A consensus approach for estimating tropical cyclone intensity from meteorological satellites: SATCON. *Wea. Forecasting*, **35**, 1645–1662, https://doi.org/10.1175/WAF-D-20-0015.1.

Wada, A., 2009: Idealized numerical experiments associated with the intensity and rapid intensification of stationary tropical-cyclone-like vortex and its relation to initial sea-surface temperature and vortex-induced sea-surface cooling. *J. Geophys. Res.*, **114**, D18111, https://doi.org/10.1029/2009JD011993.

Wang, Y., 2001: An explicit simulation of tropical cyclones with a triply nested movable mesh primitive equation model: TCM3. Part I: Model description and control experiment. *Mon. Wea. Rev.*, **129**, 1370–1394, https://doi.org/10.1175/1520-0493(2001)129<1370:AESOTC>2.0.CO;2.

——, 2002a: Vortex Rossby waves in a numerically simulated tropical cyclone. Part I: Overall structure, potential vorticity, and kinetic energy budgets. *J. Atmos. Sci.*, **59**, 1213–1238, https://doi.org/10.1175/1520-0469(2002)059<1213:VRWIAN>2.0.CO;2.

——, 2002b: Vortex Rossby waves in a numerically simulated tropical cyclone. Part II: The role in tropical cyclone structure and intensity changes. *J. Atmos. Sci.*, **59**, 1239–1262, https://doi.org/10.1175/1520-0469(2002)059<1239:VRWIAN>2.0.CO;2.

——, and C.-C. Wu, 2004: Current understanding of tropical cyclone structure and intensity changes—A review. *Meteor. Atmos. Phys.*, **87**, 257–278, https://doi.org/10.1007/s00703-003-0055-6.

Weatherford, C. L., and W. M. Gray, 1988: Typhoon structure as revealed by aircraft reconnaissance. Part II: Structural variability. *Mon. Wea. Rev.*, **116**, 1044–1056, https://doi.org/10.1175/1520-0493(1988)116<1044:TSARBA>2.0.CO;2.

Willoughby, H., 1990: Temporal changes of the primary circulation in tropical cyclones. *J. Atmos. Sci.*, **47**, 242–264, https://doi.org/10.1175/1520-0469(1990)047<0242:TCOTPC>2.0.CO;2.

——, 1998: Tropical cyclone eye thermodynamics. *Mon. Wea. Rev.*, **126**, 3053–3067, https://doi.org/10.1175/1520-0493(1998)126<3053:TCET>2.0.CO;2.

——, J. Clos, and M. Shoreibah, 1982: Concentric eye walls, secondary wind maxima, and the evolution of the hurricane vortex. *J. Atmos. Sci.*, **39**, 395–411, https://doi.org/10.1175/1520-0469(1982)039<0395:CEWSWM>2.0.CO;2.

Yang, B., Y. Wang, and B. Wang, 2007: The effect of internally generated inner-core asymmetries on tropical cyclone potential intensity. *J. Atmos. Sci.*, **64**, 1165–1188, https://doi.org/10.1175/JAS3971.1.

Yang, X., X. Zhou, X. Li, and Z. Li, 2017: Tropical cyclone wind field reconstruction from SAR and analytical model. *Hurricane Monitoring with Spaceborne Synthetic Aperture Radar*, Springer, 69–84.

Zabolotskikh, E. V., N. Reul, and B. Chapron, 2015: Geophysical model function for the AMSR2 C-band wind excess emissivity at high winds. *IEEE Geosci. Remote Sens. Lett.*, **13**, 78–81, https://doi.org/10.1109/LGRS.2015.2497463.

Zhang, B., and W. Perrie, 2017: High wind speed retrieval from multi-polarization SAR. *Hurricane Monitoring with Spaceborne Synthetic Aperture Radar*, Springer, 85–98.

Zhang, G., W. Perrie, X. Li, and J. A. Zhang, 2016: A hurricane morphology and sea surface wind vector estimation model based on C-band cross-polarization SAR imagery. *IEEE Trans. Geosci. Remote Sens.*, **55**, 1743–1751, https://doi.org/10.1109/TGRS.2016.2631663.

Zhang, J. A., and X. Li, 2017: Tropical cyclone multiscale wind features from spaceborne synthetic aperture radar. *Hurricane Monitoring with Spaceborne Synthetic Aperture Radar*, Springer, 25–39.

Zheng, G., J. Yang, A. K. Liu, X. Li, W. G. Pichel, S. He, and S. Yu, 2017: Observing typhoons from satellite-derived images. *Hurricane Monitoring with Spaceborne Synthetic Aperture Radar*, Springer, 183–214.